Universidade de Brasília – UnB

Faculdade do Gama

Programa de Pós-Graduação em Integridade de Materiais da Engenharia

Role of Lagrangian Vortices as Material Transport Barriers in a Model of Tokamak Plasmas

Ana Luiza Piragibe Freire

Advisor: Prof. Dr. Rodrigo Andrés Miranda Cerda

UNIVERSIDADE DE BRASÍLIA – UNB
FACULDADE DO GAMA

ROLE OF LAGRANGIAN VORTICES AS MATERIAL TRANSPORT BARRIERS IN A MODEL OF TOKAMAK PLASMAS

ANA LUIZA PIRAGIBE FREIRE

ADVISOR: PROF. DR. RODRIGO ANDRÉS MIRANDA CERDA

MASTER THESIS IN INTEGRITY OF MATERIALS ENGINEERING
ISSUE: 187A/2024

BRASÍLIA/DF, DECEMBER 2023

UNIVERSIDADE DE BRASÍLIA – UNB

FACULDADE DO GAMA

PROGRAMA DE PÓS-GRADUAÇÃO EM INTEGRIDADE DE MATERIAIS DA ENGENHARIA

ROLE OF LAGRANGIAN VORTICES AS MATERIAL TRANSPORT BARRIERS IN A MODEL OF TOKAMAK PLASMAS

ANA LUIZA PIRAGIBE FREIRE

MASTER'S THESIS SUBMITTED TO THE POSTGRADUATE PROGRAM IN INTEGRITY OF MATERIALS ENGINEERING AT UNIVERSITY OF BRASILIA, AS PART OF THE REQUIREMENTS FOR OBTAINING A MASTER'S DEGREE.

APPROVED BY:

PROF. DR. RODRIGO ANDRÉS MIRANDA CERDA
ADVISOR

PROF. DR. JUAN PABLO SALAZAR
EXAMINER - FEDERAL UNIVERSITY OF SANTA CATARINA

PROF. DR. ERICO LUIZ REMPEL
EXAMINER - AERONAUTICS INSTITUTE OF TECHNOLOGY

Relatório (ata) de defesa de dissertação assinado eletronicamente pela banca avaliadora, via Sistema Eletrônico de Informações - SEI, documento xxx, processo xxx.

BRASÍLIA/DF, DECEMBER 2023

CATALOGRAPHIC CARD

PIRAGIBE FREIRE, ANA LUIZA
Role of Lagrangian Vortices
as Material Transport Barriers in a Model of Tokamak Plasmas
[Distrito Federal], 2023.
54p., 210 × 297 mm (FGA/UnB Gama, Master in Integrity of Materials Engineering, 2023).
Master Thesis - Universidade de Brasília.
Faculdade do Gama
1. Physics of Plasma 2. Nuclear Fusion
3. Material Transport Barriers 4. Computational Mechanics
I. ENC/FGA/UnB. II. Title (series)

REFERENCE

PIRAGIBE FREIRE, ANA LUIZA (2023). Role of Lagrangian Vortices as Material Transport Barriers in a Model of Tokamak Plasmas. Master's Thesis in Integrity of Engineering Materials, Publication 187A/2024, Postgraduate Program, Faculty of Gama, University of Brasília, Brasília, DF, 54p.

ASSIGNMENT OF RIGHTS

AUTHOR: Ana Luiza Piragibe Freire

TITLE: Role of Lagrangian Vortices as Material Transport Barriers in a Model of Tokamak Plasmas

DEGREE: Master

YEAR: 2023

alpiragibe@gmail.com
Brasília, DF – Brazil

ACKNOWLEDGEMENTS

I would like to thank Coordination for the Improvement of Higher Education Personnel (CAPES) for the financial support.

RESUMO

PAPEL DOS VÓRTICES LAGRANGIANOS COMO BARREIRAS DE TRANSPORTE DE MATERIAIS EM UM MODELO DE PLASMAS DE TOKAMAK

No plasma de fusão, simulações numéricas são comumente utilizadas para investigar as propriedades de confinamento do plasma na região de borda dos tokamaks. As equações modificadas de Hasegawa-Wakatani (MHW) são usadas para modelar o comportamento do plasma, o que nos permite entender o transporte radial em simulações numéricas bidimensionais de turbulência de ondas de deriva resistivas eletrostáticas. Ao utilizar as equações de MHW, obtivemos melhor entendimento sobre as transições de confinamento baixo-para-alto (L-H) que ocorrem espontaneamente no plasma quando o mesmo passa de um estágio de baixo confinamento, caracterizado por fluxo turbulento, para um regime que suprime a turbulência conhecido como fluxo zonal. Para investigar essas transições, variamos o valor de um parâmetro de controle α, que está relacionado à adiabaticidade, em simulações numéricas, e observamos a transição entre os dois regimes. Este modelo simplificado de transições L-H pode fornecer informações valiosas para tokamaks. As propriedades de mistura caótica do fluxo são caracterizadas por meio de estruturas coerentes Lagrangeanas (LCS). Primeiro, calculamos o expoente de Lyapunov de tempo finito (FTLE) do campo de velocidade calculado derivado do potencial eletrostático para melhor caracterizar a mistura caótica dos regimes de fluxo turbulento e zonal. Em seguida, comparamos as estatísticas da mistura caótica dos dois regimes utilizando funções de distribuição de probabilidade (PDFs). Por fim, identificamos os vórtices Lagrangeanos utilizando a teoria geodésica para aprofundar a nossa compreensão da mistura caótica dos dois regimes, implementando também o cálculo da energia cinética para os vórtices e domínio total. Estes resultados podem contribuir para a compreensão dos processos de transporte turbulento em plasmas de fusão por confinamento magnético.

Palavras-chave: plasma de fusão, confinamento baixo-a-alto, estruturas coerentes Lagrangeanas, Expoente de Lyapunov de tempo-finito, barreiras de transporte de materiais.

ABSTRACT

In fusion plasma, numerical simulations are commonly employed to investigate the confinement properties of plasma in the bulk region of tokamaks. The modified Hasegawa-Wakatani (MHW) equations are used to model the behavior of plasma, which enables us to understand the radial transport in two-dimensional numerical simulations of electrostatic resistive drift-wave turbulence. By utilizing the MHW equations, we have gained insights into the low-to-high confinement (L-H) transitions that occur spontaneously in the plasma when it moves from a low confinement stage, characterized by turbulent flow, to a turbulence-suppressed regime known as zonal flow. To investigate these transitions, we vary the value of a control parameter α, which is related to adiabaticity, in numerical simulations, and observe the transition between the two regimes. This simplified model of L-H transitions can provide valuable information for tokamaks. The chaotic mixing properties of the flow are characterized by means of Lagrangian coherent structures (LCS). First, we compute the finite-time Lyapunov exponent (FTLE) of the calculated velocity field derived from the electrostatic potential to better characterize the chaotic mixing of the turbulent and zonal flow regimes. Then, we compare the statistics of the chaotic mixing of the two regimes using probability distribution functions (PDFs). Lastly, we identify the Lagrangian vortices using geodesic theory to further our understanding of the chaotic mixing of the two regimes, by also implementing the calculation of the kinetic energy for the vortices and total domain. These results can contribute to the understanding of turbulent transport processes in magnetic confinement fusion plasmas.

Keywords: fusion plasma, low-to-high confinement, Lagrangian coherent structures, finite-time Lyapunov exponent, material transport barriers.

Contents

List of Tables

List of Figures

LIST OF NOMENCLATURES AND ABBREVIATIONS

MHD Magnetohydrodynamics

LCFS *last closed (magnetic) flux surface*

SOL *scrape-off layer*

L low-confinement

H high-confinement

L-H low-to-high confinement

KH Kelvin-Helmholtz

HW Hasegawa-Wakatani

MHW modified Hasegawa-Wakatani

LCS Lagrangian coherent structures

FTLE finite-time Lyapunov exponents

PDFs probability distribution functions

ODEs first-order ordinary differential equations

1 INTRODUCTION

Due to global population growth and industrialization, the world's growing energy dependency has become a pressing concern. This concern revolves around our energy supply, as fossil fuels, a finite resource and significant contributor to climate change, emphasize the issue. Consequently, there is an escalating need for a clean, safe, and carbon-neutral form of electricity generation (Dewhurst, 2010). Nuclear fusion has gained recognition as an alternative solution for both energy dependency challenges and climate change. As a result, fusion reactors are being constructed worldwide, exemplified by projects like ITER in France and the recently inaugurated JT-60SA in Japan.

Nuclear fusion occurs in the interior of stars. Fusion reactions, wherein nuclei fuse together, power the Sun, producing a mass that is smaller than the combined mass of the reactants. This small mass loss results in released energy (Dewhurst, 2010). There are ongoing efforts to reproduce fusion reactions in experimental facilities. In laboratory experiments, there are two main methods to recover the energy from fusion collision, namely, magnetic confinement and inertial fusion (Chen, 2016).

In magnetic confinement devices, a magnetic field is employed to take advantage of the forces acting on charged particles in plasmas for their confinement (Dewhurst, 2010). A plasma is an ionized gas or a quasineutral gas of charged and neutral particles exhibiting collective behavior (Chen, 2016) and serves as the required fuel for fusion to occur. The tokamak is a fusion reactor regarded as one of the most promising magnetic confinement devices to achieve energy production from thermonuclear fusion.

When investigating fusion plasma, turbulent processes pose a substantial engineering challenge, because they are responsible for the radial transport toward the edge of a tokamak, which leads to plasma loss to the walls (Farge *et al.*, 2006). A fundamental challenge of fusion research is to understand the dynamics of turbulent radial particle transport and heat flux in magnetized plasmas because it holds the potential to enhance the confinement characteristics of fusion devices, including tokamaks (Bos *et al.*, 2008). Numerical simulations are a valuable tool to model this behavior, allowing the study of the overall plasma dynamics within the bulk region.

In this thesis, we employ numerical simulations of a fluid model of turbulence in fusion plasmas that displays a low-to-high confinement (L-H) transition, which is a transition observed in experiments with fusion plasmas. Spontaneously occurring, these transitions occur as the plasma shifts from a low confinement regime, referred to as turbulent flow, to a turbulence-suppressed state characterized by the presence of zonal flows, resulting in a high confinement regime. The significance of this transition lies in its capacity to enhance confinement (Numata *et al.*, 2007), making the study of L-H transitions an avenue for advancing nuclear fusion.

Turbulence can be defined as the coexistence between advecting coherent structures and random fluctuations of the velocity fluid (Davidson, 2015). The Hasegawa-Wakatani equations, employed in two-dimensional numerical simulations of electrostatic resistive drift-wave turbulence, aid in comprehending radial transport. The detection of Lagrangian coherent structures (LCSs) in turbulent flows has received much attention since the last two decades (Haller, 2001; Beron-Vera *et al.*, 2010). Furthermore, the computation of the finite-time Lyapunov exponent (FTLE), in conjunction with the utilization of Geodesic Theory, is employed to identify Lagrangian coherent structures (LCS). These approaches contribute to a more comprehensive understanding of chaotic mixing during the L-H transition.

This thesis is organized as follows. Chapter 2 provides the theoretical background on plasma and nuclear fusion. Chapter 3 describes the model employed and the numerical tools. Chapter 4 presents the numerical results, and Chapter 5 provides the conclusion.

1.1 OBJECTIVE

1.1.1 General Objective

This thesis aims to characterize the chaotic mixing properties within a simplified two-dimensional model of a tokamak undergoing a transition from low-to-high confinement. The investigation employs numerical simulations based on the modified Hasegawa-Wakatani equations. Lagrangian coherent structures are identified through the application of finite-time Lyapunov exponent and the Geodesic theory approach, focusing on electrostatic resistive drift-wave turbulence.

1.1.2 Specific Objective

- To acquire the electrostatic potential patterns (φ) from the modified Hasegawa-Wakatani equations, using two variations in the parameter α, to display the turbulent and zonal flow regime.
- To calculate the particle density flux and kinetic energy of the whole domain for both turbulent regime and zonal flow.
- To identify the material transport barriers, known as Lagrangian coherent structures (LCS), in both turbulent regime and zonal flow, using finite-time Lyapunov exponent (FTLE) approach.
- To use FTLE results to calculate the probability distribution functions (PDFs) of both regimes as to compare and to further characterize the chaotic mixing.

- To identify LCS vortices, in both turbulent regime and zonal flow, using Geodesic theory approach.
- To calculate the kinetic energy of the vortices identified in both of the regimes.

2 PLASMA AND THERMONUCLEAR FUSION

2.1 PLASMA AND ITS CRITERIA

In a gaseous state, atoms exhibit a distribution of thermal energies, and an atom undergoes ionization when subjected to a collision of sufficient kinetic energy to dislodge one of its electrons. Upon ionization, an atom retains its charge until it encounters an electron, at which point it undergoes recombination with the electron, reverting to a neutral state. The rate at which this occurs is known as the recombination rate, and it is dependent on the density of electrons (n_e), where n_e is interpreted as equal to the density of ionized atoms (n_i). The low recombination rate establishes one of the distinguishing characteristics separating plasma from other ionized gases (Chen, 2016).

Plasma is distinguished from any ionized gas by its unique characteristics, as it is defined as "a quasineutral state of matter composed of charged and neutral particles that manifest collective behavior" (Chen, 2016). The "quasineutral" component of plasma is a result of electrons exhibiting greater mobility than ions, mainly due to their lower mass, which promptly screens out any charge imbalance through the swift motion of electrons, ultimately establishing the plasma's predominant state of neutrality (Dewhurst, 2010). This implies that the quasineutrality of plasma is sufficiently neutral that $n \simeq n_e \simeq n_i$, where n is a common density called plasma density, yet not to the extent that all the electromagnetic forces cease to exist (Hazeltine and Meiss, 2003).

The concept of "collective behavior" applies to motions that are not solely influenced by local conditions but are also affected by the state of the plasma in remote regions. Plasma, containing charged particles, possesses the ability to generate local accumulations of positive or negative charges as these particles move, thereby leading to the rise of electric fields. The movement of charges also results in the generation of electric current, and subsequently, the induction of a magnetic field. The long-range electromagnetic forces significantly surpass the forces resulting from local collisions, leading to the fields' capacity to influence the motion of charged particles at a distance (Chen, 2016).

This relationship among the electric field, current, and magnetic field is summarized in Maxwell's equations of Ampere's law including displacement current, and Faraday's law (Young *et al.*, 2012),

$$\oint \vec{\boldsymbol{B}} \cdot d\vec{\boldsymbol{l}} = \mu_0 \left(i_c + \epsilon_0 \frac{d\Phi_E}{dt} \right)_{encl}, \tag{2.1}$$

$$\oint \vec{\boldsymbol{E}} \cdot d\vec{\boldsymbol{l}} = -\frac{d\Phi_B}{dt}, \tag{2.2}$$

where $\vec{\boldsymbol{B}}$ is the magnetic field,$\vec{\boldsymbol{E}}$ is the electric field, $d\vec{\boldsymbol{l}}$ is the length vector, ϵ_0 and μ_0 are, respectively, the permittivity and permeability of free space. The i_c is the conduction current, Φ_E is the electric flux, Φ_B is the magnetic flux, and $\epsilon_0 d\Phi_E/dt$ is the displacement current. The $encl$ means it has been enclosed within the surface. Eq. 2.2 corresponds to Ampere's law including displacement current, and Eq. 2.1 corresponds to Faraday's law. When we introduce the definition of electric flux and magnetic flux as $\Phi_E = \int \vec{\boldsymbol{E}} \cdot d\vec{\boldsymbol{A}}$ and $\Phi_B = \int \vec{\boldsymbol{B}} \cdot d\vec{\boldsymbol{A}}$, respectively, and assume it's in empty space, where $i_c = 0$, we can finally substitute into Eqs. 2.1 and 2.2 (Young *et al.*, 2012),

$$\oint \vec{\boldsymbol{B}} \cdot d\vec{\boldsymbol{l}} = \mu_0 \epsilon_0 \frac{d}{dt} \int \vec{\boldsymbol{E}} \cdot d\vec{\boldsymbol{A}}, \tag{2.3}$$

$$\oint \vec{\boldsymbol{E}} \cdot d\vec{\boldsymbol{l}} = -\frac{d}{dt} \int \vec{\boldsymbol{B}} \cdot d\vec{\boldsymbol{A}}, \tag{2.4}$$

as to arrive at the aforementioned relationship, where $\vec{\boldsymbol{A}}$ is the vector area.

While it may not be readily evident, Maxwell's equations encompass all the fundamental relationships between electromagnetic fields and their sources. When we incorporate the equations defining the electric and magnetic fields in terms of the forces they exert on charges,

$$\vec{F} = q\left(\vec{E} + \vec{v} \times \vec{B}\right), \tag{2.5}$$

we encompass all the foundational relationships of electromagnetism, known as the Lorentz force Law (Eq.2.5) (Gallagher, 2013). The Lorentz force represents the influence of a force ($\vec{F}$) exerted on a charged particle (q) moving with velocity ($\vec{v}$) through an electric field ($\vec{E}$) and magnetic field ($\vec{B}$). This law will serve as a fundamental concept for comprehending motion within an electromagnetic field.

A plasma can, also, be conceptualized as a colloidal suspension of charged particles that interact with and generate electromagnetic fields. In the absence of an electric field and under the influence of a uniform magnetic field, charged particles will exhibit helical motion along magnetic field lines. This is illustrated by disassembling Eq 2.5 and decomposing the uniform velocity into its constituent components aligned parallel ($\vec{v_{||}}$) and perpendicular ($\vec{v_\perp}$) to the magnetic field ($\vec{B}$),

$$\vec{F} = q\vec{v_\perp} \times \vec{B}. \tag{2.6}$$

Since there is no parallel force to the magnetic field (v x B equals zero), the particles are unrestricted in their movement along the magnetic field lines. The perpendicular force, however, applies force that acts both perpendicular to the magnetic field lines and the particle's velocity.

As a result, the particle follows a helical path, moving along the magnetic field and undergoing rapid simple harmonic oscillations, a phenomenon referred to as gyration. This gyration is characterized by the gyrofrequency, also known as the cyclotron frequency (ω_c), is given by (Dewhurst, 2010; Gallagher, 2013; Chen, 2016),

$$\omega_c = \frac{qB}{m}. \tag{2.7}$$

While, the equation for the radius of the circular particle motion that orbits the field line, also known as the Larmor radius (r_L), is given by (Chen, 2016; Dewhurst, 2010; Gallagher, 2013),

$$r_L = \frac{mv_\perp}{qB}, \tag{2.8}$$

where m is the mass of the particle, $v_\perp$ is the velocity perpendicular to the field line.

In the presence of an electric field, the particle's motion becomes a composite of two elements: the conventional circular Larmor gyration and a drift of the guiding center. The drift is aligned with both the magnetic and electric fields, and it is denoted as the $\vec{E} \times \vec{B}$ drift. The guiding center of the particle will drift with a velocity ($v_{\vec{E}}$),

$$v_{\vec{E}} = \frac{\vec{E} \times \vec{B}}{B^2}. \tag{2.9}$$

The drift is unaffected by the mass and charge of individual particles, resulting in the entire plasma drifting in this direction. This Equation 2.9 serves as a fundamental component of the guiding center drifts of plasma particles and plays a pivotal role in the physics of magnetic confinement. This phenomenon will be discussed in greater detail in Section 2.2.2.

For now, we define the three distinct criteria that plasma must adhere to differentiate from other ionized gases, which will be discussed in the following sections, Debye Shielding (Section 2.1.1), Debye Sphere (Section 2.1.2), and Collision Frequency (Section 2.1.3).

2.1.1 Debye Shielding

A fundamental characteristic of plasma behavior lies in its capacity to shield out applied electric potentials (Chen, 2016). This phenomenon is referred to as Debye Shielding, and it is this shielding mechanism that ensures the quasineutrality of plasma, as described in the preceding section. Due to the presence of freely roaming charged particles in plasma, the application of any electric potential results in the accumulation of charged particles around this potential, giving rise to this shielding effect.

However, due to thermal motion driven by the finite thermal energy, particles located at the edge of the shielding cloud, where the electric field is relatively weak, possess sufficient thermal energy to overcome the electrostatic potential well and escape, leading to an imperfect shielding. The extent of the edge of the shielding cloud is determined by a radius at which the

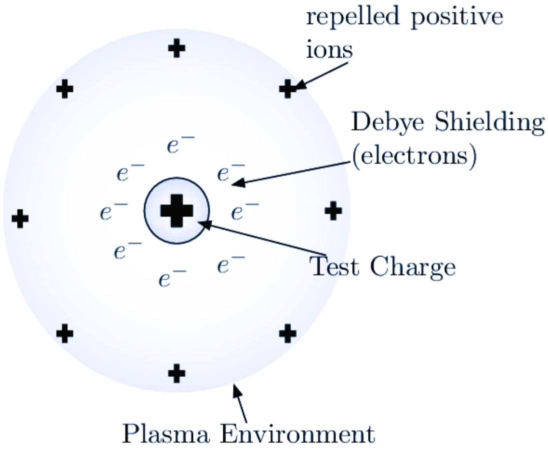

Figure 2.1. Debye Shielding. Source: (Schaub *et al.*, 2006)

potential energy is roughly equivalent to the thermal energy of the particles. This measurement of the shielding distance or thickness of the sheath is referred to as the Debye length (λ_D) (Wesson and Campbell, 2004),

$$\lambda_D \equiv \left(\frac{\epsilon_0 K T_e}{n e^2}\right)^{1/2}, \tag{2.10}$$

where ϵ_0, K and e are constants, known as, respectively, the permittivity of free space, the Boltzmann's constant and the charge of an electron. The T_e is the electron temperature and n is the number density. As anticipated, an increase in density results in a decrease in the λ_D. Furthermore, the λ_D increases with the rise in thermal energy, represented by KT_e. In the absence of thermal agitation, the charge cloud would condense into an infinitely thin layer. The electron temperature is incorporated into the definition of the Debye length due to the fact that electrons, being more mobile than ions, primarily contribute to the shielding by their motion, leading to the creation of an excess or deficit of negative charge (Hazeltine and Meiss, 2003).

The first criterion for an ionized gas to be classified as a plasma is that it must possess sufficient density such that the λ_D is significantly smaller than L (Crepaldi, 2021; Chen, 2016),

$$\lambda_D \ll L, \tag{2.11}$$

where L is the dimension of a system. This implies that, in summary, Debye shielding must ensure that the sheath's thickness is several orders of magnitude smaller than the system's dimensions, thereby preserving the quasineutral state of the majority of the plasma by ensuring that the majority of the plasma remains free of significant electrostatic potentials and electric fields.

2.1.2 Debye Sphere

The second criterion that distinguishes plasma from other ionized gases is associated with its collective behavior. The Debye Shield depicted in Fig. 2.1 is only applicable when a sufficient number of particles are present to create a charged cloud around the applied potential, often referred to as the Debye Sphere. If there are only one or two particles present in the sheath region, the statistical validity of Debye shielding would be unfounded. The calculation of the number of particles N_D present in the Debye Sphere is determined by (Souza, 2012),

$$N_D = n\frac{4\pi}{3}\lambda_D^3, \tag{2.12}$$

where n is the plasma density and λ_D is the Debye length. This implies that, in addition to $L \gg \lambda_D$, plasma particles interact with a large number of other particles, ensuring the collective behavior (Chen, 2016),

$$N_D \ggg 1. \tag{2.13}$$

2.1.3 Collision Frequency

The final criterion that an ionized gas must meet to be classified as a plasma pertains to a condition related to collisions. If the charged particles experience collisions with neutral atoms at such a high frequency that their motion is governed by conventional hydrodynamic forces rather than electromagnetic forces, then the ionized gas does not qualify as plasma. For charged particles to be primarily governed by electromagnetic forces, it is necessary that the typical frequency of plasma oscillations (ω_p) exceeds the frequency at which these particles collide with neutral atoms (Gallagher, 2013),

$$\omega_p \tau_c > 1, \tag{2.14}$$

where τ_c is is the mean time between collisions with neutral atoms. If this phenomenon does not take place, and collisions with neutral particles dominate, the ionized gas would transition to a neutral state.

The frequency of plasma oscillation (Souza, 2012),

$$\omega_p = \left(\frac{ne^2}{m\epsilon_0}\right)^{1/2}, \tag{2.15}$$

is a cyclical process that leads to the generation of plasma waves. This occurs because when a plasma is perturbed, its charged particles acquire kinetic energy through acceleration induced by the local electric field created in response to the perturbation. The electric field drives the motion of charged particles, resulting in the reversal of both the direction of the field and the direction of acceleration. Electrons endeavor to neutralize positive charges, and due to inertia, they traverse beyond the point, leading to a periodic reversal of the direction of both the electric field and their movement. This reversal is a consequence of plasma's macroscopic neutrality, often referred to as its quasineutrality.

2.2 CONTROLLED THERMONUCLEAR FUSION

The terminology 'thermonuclear' is derived from plasma being in a state of thermal equilibrium (Chen, 2016), whereas the label 'controlled' is associated with the utilization of the thermonuclear reaction as a manageable and sustainable energy source contributing to the energy matrix (Crepaldi, 2021). As previously mentioned, the fusion process occurs naturally in the sun, and substantial efforts have been invested in making it attainable on Earth. It is noteworthy that, in contrast to nuclear fission, fusion reactions do not entail the risk of catastrophic runaway events and result in minimal radioactive waste generation. Any radioactive waste that does arise typically consists of small quantities of short-lived isotopes resulting from neutron bombardment and the activation of the fusion device (Dewhurst, 2010).

To make fusion viable on Earth, one approach is to increase the inertia of the reaction through head-on collisions with heavier isotopes. This heightened inertia is critical for overcoming the electric repulsion of ions with like charges. Overcoming an electric potential barrier is a necessity for the fusion reaction to progress, with the barrier's magnitude contingent upon the specific reactants involved. The most promising reaction is the fusion of deuterium (D) and tritium (T) to produce a neutron and a helium nucleus (or an alpha particle) (Kikuchi *et al.*, 2012),

$$D + T \rightarrow He(3.5MeV) + n(14.1MeV) \tag{2.16}$$

where the fuel is composed of heavy hydrogen isotopes, specifically deuterium with one proton and one neutron and tritium with one proton and two neutrons. Deuterium exists naturally, constituting approximately one part in 6000 of water (Chen, 2016). In the fusion reaction, the mass disparity between deuterium and tritium ($D + T$), resulting in the formation of an alpha particle (He), corresponds to a difference of 0.01875 proton masses (Gallagher, 2013). This discrepancy gives rise to the liberation of 17.6 MeV of energy, as calculated by the equation $E = Mc^2$ (Chen, 2016).

There are two primary methods for harnessing energy from D-T fusion reactions: magnetic confinement and inertial fusion. This thesis predominantly explores magnetic confinement. In the context of the D-T fusion reaction, the majority of energy is carried by the 14.1-MeV neutron, while the 3.5-MeV alpha particle is trapped within the magnetic field confining the plasma. By confining plasma within a magnetic field, both ions and electrons achieve thermal equilibrium characterized by Maxwellian distributions. (Wesson and Campbell, 2004). Consequently, any energy gained or lost during electric collisions is reabsorbed into the thermal distribution. Achieving this thermal equilibrium requires heating the plasma to extremely high temperatures, making confinement by a physical wall unfeasible. Instead, magnetic fields are utilized to confine the plasma and keep it isolated from the walls of a vacuum chamber. These walls are maintained under near-vacuum conditions by adjusting the magnetic field to balance the internal plasma pressure.(Gallagher, 2013).

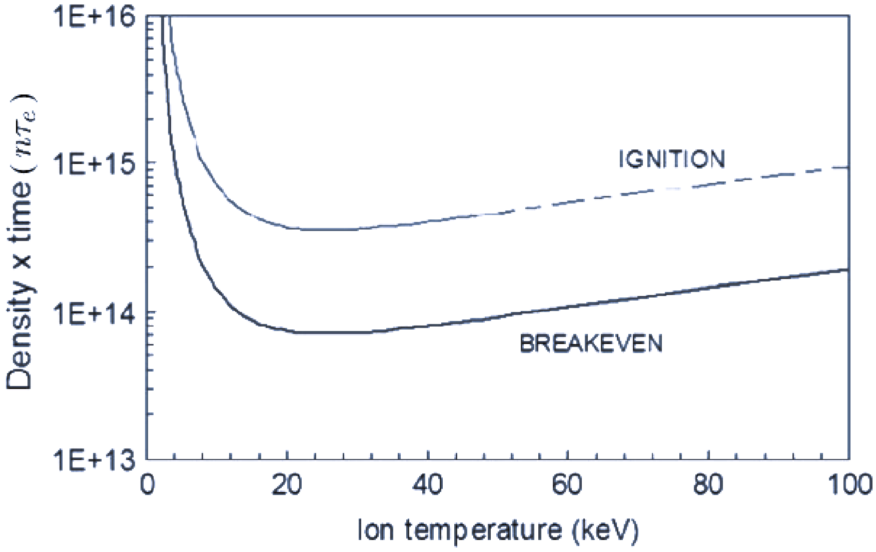

Figure 2.2. The Lawson criterion product for D-T fusion. Adapted from source: (Chen, 2016)

There are two principal methods to surpass the Lawson criterion, one of which is magnetic confinement. The Lawson criterion(Lawson, 1957; Dewhurst, 2010),

$$n\tau_e \tag{2.17}$$

defined by the product of the density of fusing nuclei (n) and the mean time for plasma energy leakage (τ_e), is a key factor for achieving breakeven and ignition in fusion (see Fig.2.2). Breakeven is attained when the fusion energy produced equals the energy used to create the plasma. In contrast, ignition occurs when the alpha particles generated by the fusion reaction are trapped within the magnetic field for a sufficient duration to maintain the plasma's temperature without the need for additional energy input. In magnetic confinement, the minimum $n\tau_e$ is attained by maintaining a dense plasma within a magnetic field for a duration of time (τ_e) (Chen, 2016).

2.2.1 Tokamak

The Tokamak is a leading approach in the pursuit of controlled nuclear fusion through magnetic confinement. It effectively traps ions and electrons engaged in Larmor orbits, enabling movement along magnetic field lines while preventing their escape through toroidal confinement. In a toroidal configuration, magnetic field lines avoid forming closed loops and instead follow irregular paths along magnetic surfaces. The torus (Figure 2.3) takes on a doughnut-like

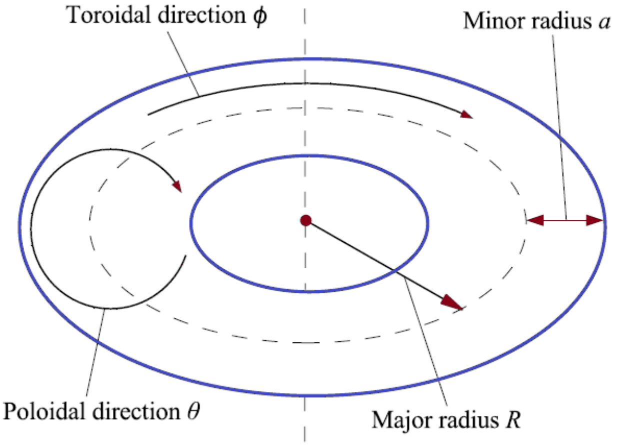

Figure 2.3. The Torus. Source: (Dewhurst, 2010)

shape, characterized by two radii: the major radius, extending from the center of rotation to the center of the circular structure, and the minor radius, defining the radius of the smaller internal circle. Within the torus, two distinct directions of movement exist: the long, toroidal direction, and the short, poloidal direction.

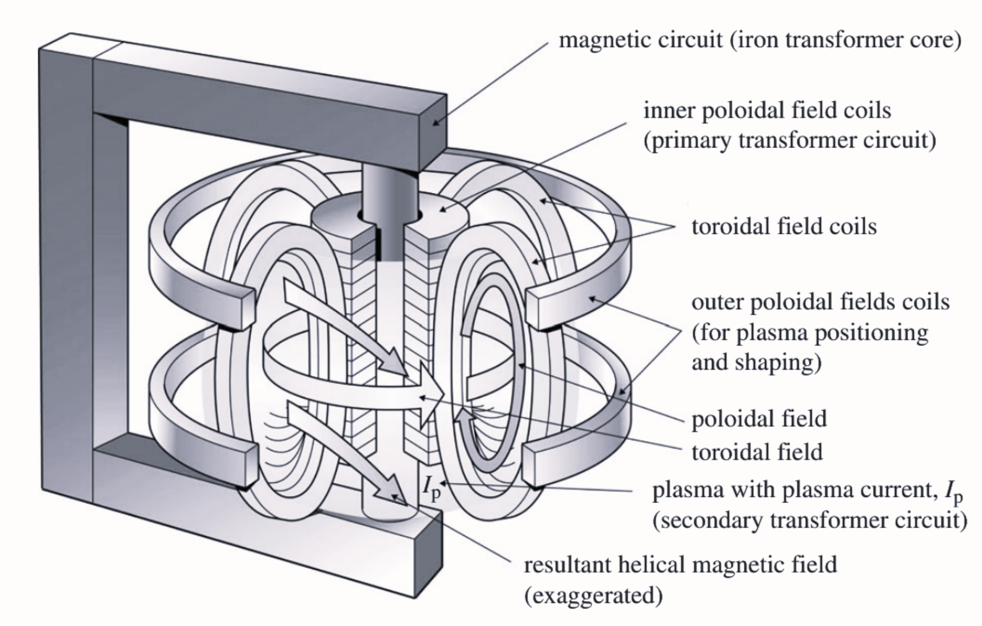

Figure 2.4. Principle of a Tokamak. Source: (Smith and Cowley, 2010)

The term ”Tokamak” is, in fact, a Russian acronym that translates to ”toroidal compartment with magnetic field coils” (Zohm, 2014). The Tokamak originated in the Soviet Union during the 1950s (Kadomtsev, 1988), with its design aimed at producing both a poloidal and a toroidal magnetic field, resulting in an overall magnetic field configuration exhibiting a helical shape (Fig.2.4), with each magnetic field line positioned on one of a nested series of toroidal flux surfaces (Wesson and Campbell, 2004), demonstrated by Fig.2.5. The employment of a helical magnetic field within a toroidal structure serves to counteract the outward pressure exerted by the plasma. This pressure equilibrium can be explained using the principles of

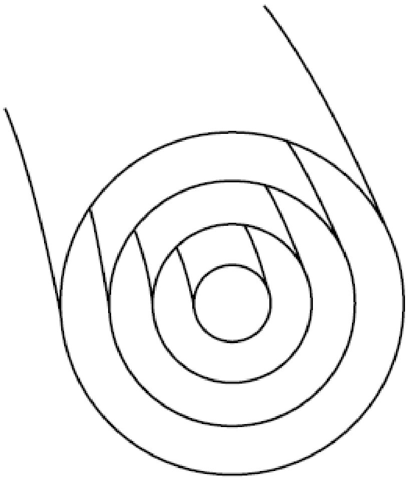

Figure 2.5. Magnetic flux surfaces forming a series of nested toroids. Source: (Stangeby *et al.*, 2000)

Magnetohydrodynamics (MHD), where the plasma is treated as a unified electrically neutral conducting fluid. This analysis aligns with the ideal MHD model, which disregards resistivity. The ideal MHD equations, also known as the simplified MHD equations (Bittencourt, 2004, p. 235), can be written as (Dendy, 1990; Bittencourt, 2004),

$$\frac{\partial \rho}{\partial t} + \nabla \cdot (\rho \vec{v}) = 0, \tag{2.18}$$

$$\rho \frac{D\vec{v}}{Dt} = \vec{J} \times \vec{B} - \nabla p, \tag{2.19}$$

$$\vec{E} = -\vec{v} \times \vec{B}, \tag{2.20}$$

$$\nabla \times \vec{B} = \mu_0 \vec{J}, \tag{2.21}$$

where ρ is the mass density, $\vec{v}$ is the mass velocity, and $\vec{J}$ is the current density. The closure of these equations is achieved by incorporating the equations of state, Faraday's Law (Eq 2.2) and Ampere's Law (Eq 2.1). The MHD describes the behaviors of magnetized plasma, primarily serving as a foundation for researching the equilibrium and stability of plasmas. The equilibrium state of the conducting fluid is attained when, utilizing the force balance equation (Eq 2.19), the pressure gradients (∇p) are balanced by the Lorentz force (Eq 2.5) (Dewhurst, 2010; Gallagher, 2013),

$$\nabla p = \vec{J} \times \vec{B} = 0. \tag{2.22}$$

This implies that $\nabla \cdot \vec{J} = 0$, which is the equation of conservation of electric charge in the absence of alterations in the overall macroscopic charge density ρ, signifying that the ρ must remain constant along both the magnetic field lines and the current lines (Bittencourt, 2004; Gallagher, 2013). In fact, the simplest geometric configuration that fulfills Lorentz force Law (Eq. 2.5) and Ampere's law is the toroidal shape (Dewhurst, 2010).

In the presence of collisions, particles undergo stochastic forces, inducing resistance to current flow. Their impact can be better understood within the framework of MHD by incorporating resistivity (η) into Eq.2.20,

$$\vec{E} + \vec{v} \times \vec{B} = \eta \vec{J}, \tag{2.23}$$

where Equation 2.23 represents the classical description of transport phenomena in a plasma tokamak. Collisions induce cross-field transport of plasma particles along the pressure gradient, leading to a decrease in confinement efficiency (Dewhurst, 2010).

The high-temperature plasma necessary for magnetic fusion needs to be effectively confined, preventing contact with the vessel wall to avoid wall melting and plasma disruption. Within a tokamak, a specifically designed region with closed magnetic lines, surrounded by open field lines, is engineered to manage significant heat and particle fluxes. These closed field lines trace paths on magnetic flux surfaces, adopting the configuration of concentric tori within the tokamak. The outermost flux surface, where the field lines are closed, is termed the *last closed (magnetic) flux surface* (LCFS) and is frequently utilized to define the plasma edge. On the other hand, the zone characterized by open magnetic field lines is identified as the *scrape-off layer* (SOL). The implementation of divertors in tokamaks is instrumental in achieving this configuration (Stangeby *et al.*, 2000), as illustrated in Fig.2.6.

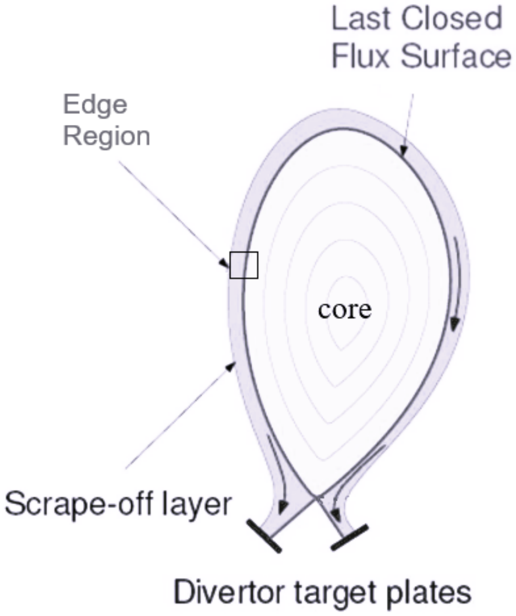

Figure 2.6. Simplified magnetic field configuration of a diverted tokamak. Adapted from source: (Kubic, 2012)

2.2.2 Edge Plasma and Turbulence

The edge region (Fig.2.6) of magnetically confined plasma presents a highly complex environment with substantial pressure gradients and intricate geometric structures. The equilibrium of pressure gradients is upheld by a strong magnetic field (Eq.2.22), serving as a source of free energy capable of instigating instabilities and turbulence. Macroscale instabilities, including MHD instabilities, can lead to plasma disruptions, resulting in the potential loss of confinement. This phenomenon appears from the capacity of turbulent motions to alter gradients through nonlinear interactions (Dewhurst, 2010).

When examining the geometric influences at the edge region, there is an increase in classical transport known as neoclassical transport (Hinton and Hazeltine, 1976). Neoclassical transport incorporates toroidal geometry and introduces an enhanced theoretical diffusion coefficient. Nonetheless, neoclassical transport falls short when compared to experimentally measured transport rates, which are consistently orders of magnitude higher (Furth, 1975). This disparity in values is referred to as anomalous transport and is commonly attributed to the presence of turbulence induced by microscale instabilities.

The treatment of turbulence in fusion plasmas often involves the consideration of drift waves and drift wave instability. Microscale instabilities, such as drift waves, are believed to be the primary contributors to anomalous transport in tokamaks (Horton, 1990; Weiland, 2000). Drift waves are characterized by low frequencies compared to the ion cyclotron frequency, and they are driven by gradients in density or temperature. In drift waves, electrons can move along the magnetic field, establishing thermodynamic equilibrium in accordance with the Boltzmann relation (Pushkarev, 2013; Dewhurst, 2010),

$$\frac{\partial n}{n} = \frac{e\partial\varphi}{T}, \tag{2.24}$$

This equation indicates that perturbations in density (n) are linked to perturbations in electrostatic potential (φ). The derivation of the governing equations for the evolution of drift waves will be explored in greater detail in section 3.1.

Plasma fluctuations resulting from drift wave instability were initially detected in linearly magnetized plasma devices (D'Angelo, 1961; Lashinsky, 1964). Resistivity contributes to the out-of-phase behavior of potential and density fluctuations, triggering drift wave instability. This instability, in turn, evolves into drift wave turbulence through nonlinear interactions. When density and potential fluctuations are out of sync, a net density flux arises, contributing to the transport of plasma along the density gradient. In tokamaks, this turbulent plasma transport is most pronounced in the edge region where gradients are substantial (Mazzucato, 1976), causing a radially outward flow and, consequently, a reduction in confinement.

2.2.3 Low-to-High Confinement Transitions

The tokamak plasma, in a quasi-two-dimensional (2D) geometry, can experience a self-induced spontaneous transition from a low-confinement (L) state to a high-confinement (H) state, entering a turbulence-suppressed regime where the formation of a transport barrier occurs at the LCFS (Horton, 1990; XU and WU, 2017). This phenomenon is recognized as the low-to-high confinement (L-H) transit and was initially discovered in 1982 (Wagner *et al.*, 1982). It is characterized by an effective enhancement of confinement achieved through the suppression of anomalous transport. The L-H transition in a tokamak is linked to the nonlinear self-generation of poloidal $\vec{E} \times \vec{B}$ shear or zonal flow in the edge region (Moyer *et al.*, 1995; Burrell, 1997). Zonal flows play a critical role in mitigating anomalous transport by absorbing energy from drift waves and disrupting the eddies responsible for turbulent transport, for this reason, zonal flows are a key factor in achieving improvements in confinement (Diamond *et al.*, 2005).

The transitions between the turbulence-dominated regime (L-mode) and the zonal-flow-dominated regime (H-mode) can be outlined through three principal governing processes: firstly, the initiation of turbulence induced by drift waves; secondly, the inherent self-organization of zonal flows; and thirdly, the destabilization of the zonal flow (Numata *et al.*, 2007). The instabilities driving these transitions correspond to a bifurcation of the momentum equilibrium at the plasma edge, instigated by alterations in neoclassical transport or momentum boundary conditions (XU and WU, 2017). The primary instability materializes at a linear stability threshold within the equilibrium featuring a zero-background flow, aligning physically with the initiation and amplification of drift waves (Connor and Wilson, 2000; Bishop, 1986; Rogers *et al.*, 1998). This instability generates the L-mode through density or temperature gradients responsible for drift waves (Fig.2.7).

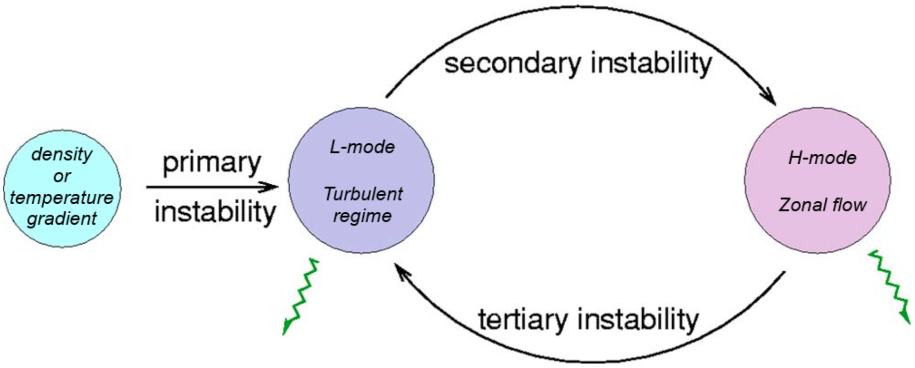

Figure 2.7. Mechanism of L-H transition. Zig-zag green arrows symbolize channels of dissipation. Adapted from source: (Numata *et al.*, 2007)

The secondary instability is responsible for the zonal flow onset (Fig.2.7). In plasmas, zonal flows manifest beyond the primary threshold, stemming from an instability in drift waves that effectively suppresses drift wave activity. Zonal flows are characterized as ”azimuthally symmetric band-like shear flows” (Diamond *et al.*, 2005)(Fig.2.8), driven by nonlinear and nonlocal interactions that facilitate the transfer of energy from drift waves to zonal flows. The transition from drift waves to zonal flows is governed by two distinct processes. The first process involves a mechanism of secondary instability, wherein small-scale turbulence drives a sheared zonal flow through a nonlinear mechanism, facilitated by an inverse cascade of energy (Kim and Diamond, 2003; Diamond *et al.*, 1994). A rapid increase in the energy transfer rate from turbulence to zonal flows is crucial, facilitated through the turbulent Reynolds stress (XU and WU, 2017).

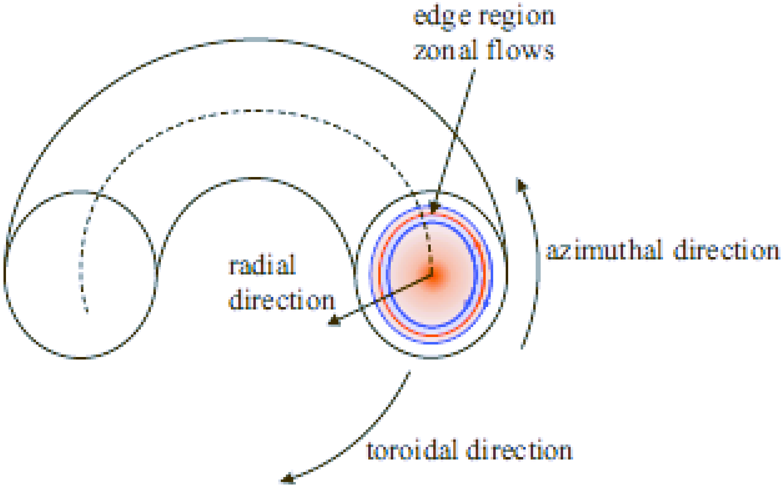

Figure 2.8. Zonal flows, in tokamaks, refer to toroidally invariant velocity fields within the azimuthal plane, localized in proximity to the plasma edge. Source: (Pushkarev, 2013)

The second process, constituting a secondary instability mechanism leading to the generation of zonal flows, involves the Kelvin-Helmholtz (KH) instability (Rogers *et al.*, 2000; Jenko *et al.*, 2000). In this context, the KH instability is instigated by radially elongated drift wave eigenmodes. The KH mode of the drift waves inherently possesses a zonal flow component, offering a natural mechanism for the growth of zonal flows (Numata *et al.*, 2007). The zonal flow functions to suppress small-scale turbulence by shearing turbulent eddies and/or drift wave packets, thereby eliminating the source of anomalously high transport and losses of plasma particles and energy (Diamond *et al.*, 2005). The total energy of drift waves and zonal flows remains conserved; thus, as the zonal flow grows, the energy of drift waves diminishes. This implies that zonal flows can store energy without inducing a deterioration in plasma confinement (Gallagher, 2013).

As zonal flows intensify, they undergo tertiary instability, leading to the disintegration of the coherent zonal structure into turbulent small-scale eddies through KH instabilities of the zonal flows. The small-scale turbulence may subsequently reorganize through secondary instabilities (Numata *et al.*, 2007) (Fig.2.7).

3 NUMERICAL METHODS

3.1 HASEGAWA-WAKATANI EQUATIONS

The Hasegawa-Wakatani (HW) equations were formulated to explore the origins of anomalous edge transport caused by collisional drift waves. These equations encompass fundamental principles for analyzing turbulence, as well as the emergence and dissipation of coherent macroscopic structures (Hasegawa and Wakatani, 1987).

Consider the edge region of a plasma magnetically confined by a uniform magnetic field $\vec{B}$ in the presence of a background density gradient ∇n_0. The ion temperature $T_i = 0$, and for the electron temperature $T_e = T = constant$. Assuming an electrostatic approximation, we have:

$$\vec{E} = -\nabla\varphi, \tag{3.1}$$

where $\vec{E}$ is the electric field and φ is the electrostatic potential. Furthermore, the plasma is in a quasinuetral state,

$$n = n_e = n_i. \tag{3.2}$$

The HW equations can be obtained by analyzing the two-fluid equations of motion in the parallel (section 3.1.3) and perpendicular directions (sections 3.1.1 and 3.1.4) with respect to the magnetic field and the continuity equations of ions and electrons (sections 3.1.5 and 3.1.4, respectively).

3.1.1 The Perpendicular Equation of Momentum of Ions

The ion equation of motion is,

$$m_i n \left(\frac{\partial}{\partial t} + \vec{v_i} \cdot \nabla\right) \vec{v_i} = -\nabla p_i + ne\left(\vec{E} + \vec{v_i} \times \vec{B}\right) - \vec{R} + \nu\nabla^2\vec{v_i} \tag{3.3}$$

where m_i is the ion mass, $\vec{v_i}$ is the velocity of ions, p_i is the pressure of ions, ν is the kinematic viscosity and $\vec{R}$ is a term that represents collisions between ions and electrons, and is given by

$$\vec{R} = -nm_e\left(\vec{v_e} - \vec{v_i}\right) f_{ei},$$

where m_e is the electron mass, $\vec{v_e}$ is the electron velocity, and f_{ei} is the frequency of Coulomb collisions between electrons and ions. Neglecting the pressure, collisions, the dissipation terms, and considering a direction perpendicular to the magnetic field, Eq.(3.3) becomes,

$$m_i n \left(\frac{\partial}{\partial t} + \vec{v_i} \cdot \nabla_\perp \right) \vec{v_i} = ne \left(-\nabla_\perp \varphi + \vec{v_i} \times \vec{B} \right), \tag{3.4}$$

where,

and

$$\nabla_\perp = \frac{\partial}{\partial x} + \frac{\partial}{\partial y}, \qquad \vec{B} = B\hat{z}.$$

The $\vec{E} \times \vec{B}$ drift velocity can be obtained by setting the left-hand side of Eq.(3.4) to zero,

$$-\nabla_\perp \varphi + \vec{v_i} \times \vec{B} = 0. \tag{3.5}$$

Taking the cross-product of Eq.(3.5) with $\vec{B}$ yields,

$$-\vec{B} \times \nabla_\perp \varphi + \vec{B} \times \left(\vec{v_i} \times \vec{B} \right) = 0. \tag{3.6}$$

Applying the identity,

$$\vec{A} \times \left(\vec{B} \times \vec{C} \right) = \left(\vec{A} \cdot \vec{C} \right) \vec{B} - \left(\vec{A} \cdot \vec{B} \right) \vec{C},$$

into Equation (3.6) we obtain,

$$-\vec{B} \times \nabla_\perp \varphi + \left(\vec{B} \cdot \vec{B} \right) \vec{v_i} - \left(\vec{B} \cdot \vec{v_i} \right) \vec{B} = 0. \tag{3.7}$$

Since,

$$\vec{v_i} = v_{ix}\hat{x} + v_{iy}\hat{y} + v_{iz}\hat{z},$$

and the term $\left(\vec{B} \cdot \vec{v_i} \right) = Bv_{iz} = Bv_{i\|}$, Eq. (3.7) becomes,

$$-B\hat{z} \times \nabla_\perp \varphi + B^2 \vec{v_i} - Bv_{i\|} \vec{B} = 0. \tag{3.8}$$

Decomposing the ion velocity into parallel and perpendicular components,

$$\vec{v_i} = \vec{v_{i\perp}} + \vec{v_{i\|}},$$

and inserting into Eq.(3.8), we obtain,

$$-B\hat{z}\times\nabla_\perp\varphi+B^2\vec{v_{i\perp}}+B^2\vec{v_{i\parallel}}-B^2v_{i\parallel}\hat{z}=0. \tag{3.9}$$

Since $v_{i\parallel}\hat{z}=\vec{v_{i\parallel}}$, Eq.(3.9) becomes,

$$\vec{v_{i\perp}}=\frac{B\hat{z}\times\nabla_\perp\varphi}{B^2}=\frac{\hat{z}\times\nabla_\perp\varphi}{B} \tag{3.10}$$

Equation (3.10) represents the perpendicular ion drift velocity ($(\vec{v_i})_{\vec{E}\times\vec{B}}$) analogous to Eq.(2.9),

$$(\vec{v_i})_{\vec{E}\times\vec{B}}=\frac{\vec{E}\times\vec{B}}{B^2}=\frac{B\hat{z}\times\nabla_\perp\varphi}{B^2}=\frac{\hat{z}\times\nabla_\perp\varphi}{B}. \tag{3.11}$$

Inserting Equation (3.11) into the left-hand side of Eq.(3.4) we obtain,

$$m_in\left(\frac{\partial}{\partial t}+(\vec{v_i})_{\vec{E}\times\vec{B}}\cdot\nabla_\perp\right)(\vec{v_i})_{\vec{E}\times\vec{B}}=ne\left(-\nabla_\perp\varphi+\vec{v_i}\times\vec{B}\right). \tag{3.12}$$

Taking the cross-product with $\vec{B}$ we obtain the next order correction of $\vec{v_{i\perp}}$.

$$\frac{m_i}{eB}\hat{z}\times\left(\frac{\partial}{\partial t}+(\vec{v_i})_{\vec{E}\times\vec{B}}\cdot\nabla_\perp\right)(\vec{v_i})_{\vec{E}\times\vec{B}}+(\vec{v_i})_{\vec{E}\times\vec{B}}=\vec{v_{i\perp}}. \tag{3.13}$$

In the presence of a temporally varying uniform electric field, a new ion velocity emerges. The first term in the left-hand side of Eq.(3.13) corresponds to the ion polarization drift velocity,

$$\vec{v_p}=-\frac{m_i}{eB^2}\frac{D}{Dt}\nabla_\perp\varphi=\frac{m_i}{eB}\frac{D}{Dt}\left[\hat{z}\times(\vec{v_i})_{\vec{E}\times\vec{B}}\right], \tag{3.14}$$

where the $D/Dt=\partial/\partial t+(\vec{v_i})_{\vec{E}\times\vec{B}}\cdot\nabla_\perp$. The polarization drift is due to the time-varying electric field. From Equations (3.13) and (3.14) we have that the perpendicular equation of momentum of ions is reduced to a velocity,

$$\vec{v_{i\perp}}=(\vec{v_i})_{\vec{E}\times\vec{B}}+\vec{v_p}. \tag{3.15}$$

3.1.2 The Perpendicular Equation of Momentum of Electrons

The electron equation of motion can be written as,

$$m_en\left(\frac{\partial}{\partial t}+\vec{v_e}\cdot\nabla_\perp\right)\vec{v_e}=-ne\left(-\nabla_\perp\varphi+\vec{v_e}\times\vec{B}\right)-T\nabla_\perp n. \tag{3.16}$$

Again, by setting the left-hand side to zero we can obtain the lowest order velocity of electrons:

$$0 = -ne\left(-\nabla_\perp \varphi + \vec{v_e} \times \vec{B}\right) - T\nabla_\perp n. \tag{3.17}$$

Taking the cross-product with $\vec{B}$ gives,

$$\begin{aligned}\vec{B} \times \vec{0} &= \vec{B} \times \left[-ne\left(-\nabla_\perp \varphi + \vec{v_e} \times \vec{B}\right) - T\nabla_\perp n\right] \\ \Rightarrow 0 &= ne\left(\vec{v_e}\right)_{\vec{E}\times\vec{B}} - ne\vec{v_{e\perp}} - nev_{ez}\hat{z} + nev_{ez}\hat{z} - T\frac{\hat{z}\times\nabla_\perp n}{B}.\end{aligned} \tag{3.18}$$

From Equation (3.18)

$$\vec{v_{e\perp}} = \left(\vec{v_e}\right)_{\vec{E}\times\vec{B}} - \frac{T}{neB}\hat{z}\times\nabla_\perp n. \tag{3.19}$$

Equation (3.19), ultimately, represents the perpendicular equation of momentum of electrons,

$$\vec{v_{e\perp}} = \left(\vec{v_e}\right)_{\vec{E}\times\vec{B}} + \vec{v_{de}}, \tag{3.20}$$

where $\vec{v_{de}}$ represents the electron diamagnetic drift velocity. The polarization drift is neglected for electrons, because $m_i \gg m_e$. The diamagnetic drift for ions is neglected, because we assumed $T_i = 0$.

Since, $\left(\vec{v_e}\right)_{\vec{E}\times\vec{B}} = \left(\vec{v_i}\right)_{\vec{E}\times\vec{B}}$ making it analogous to $\vec{v_E}$ (Eq.(2.9)), we can rewrite the perpendicular equations of momentum of ions and electrons as,

$$\vec{v_{i\perp}} = \vec{v_E} + \vec{v_p}, \tag{3.21}$$

$$\vec{v_{e\perp}} = \vec{v_E} + \vec{v_{de}}. \tag{3.22}$$

3.1.3 The parallel momentum

The ions are assumed to be immobile in the parallel direction with reference to the magnetic field. Therefore, the parallel dynamics are dominated by the electrons. Neglecting the inertial term, the equation of motion of electrons parallel to the magnetic field can be written as,

$$\begin{aligned}m_e n\left(\frac{\partial}{\partial t} + \vec{v_e}\cdot\frac{\partial \hat{z}}{\partial z}\right)\vec{v_e} &= -\frac{\partial p_e}{\partial z} + ne\left(\frac{\partial}{\partial z}\varphi\hat{z} + \vec{v_e}\times\vec{B}\right) + \vec{R} \\ \Rightarrow 0 &= -\frac{\partial p_e}{\partial z} + ne\left(\frac{\partial}{\partial z}\varphi\hat{z} + \vec{v_e}\times\vec{B}\right) + \vec{R}.\end{aligned} \tag{3.23}$$

The electrical resistivity is a measurement of how strongly a given material opposes the flow of electric current. Here, we introduce the Spitzer resistivity,

$$\eta = \frac{m_e}{ne^2} f_{ei}.$$

The collision term can be rewritten as,

$$\vec{R} = en\eta\vec{J}. \tag{3.24}$$

where $\vec{J} = ne\left(\vec{v_i} - \vec{v_e}\right)$. Note that $J_z = -nev_{ez}$. Substituting Equations (3.24) into (3.23) we obtain,

$$0 = -\frac{\partial p_e}{\partial z} + ne\left(\frac{\partial}{\partial z}\varphi\hat{z} + \vec{v_e} \times \vec{B}\right) + en\eta J_z\hat{z}. \tag{3.25}$$

From Equation (3.25) we obtain the parallel current density,

$$en\eta J_z = \frac{\partial p_e}{\partial z} - ne\frac{\partial}{\partial z}\varphi. \tag{3.26}$$

From the state equation of electrons $p_e = n_e T = nT$, also known as the electron pressure, we obtain,

$$J_z = \frac{T}{e\eta}\left(\frac{1}{n}\frac{\partial n}{\partial z} - \frac{e}{T}\frac{\partial \varphi}{\partial z}\right). \tag{3.27}$$

The parallel electron motion (J_z) plays a crucial role in initiating, maintaining, and disrupting zonal flow. The electron's parallel response, as described by the generalized Ohm's law, results in the resistive coupling between the electrostatic potential (φ) and the density fluctuations (n).

3.1.4 The electron continuity equation

For electrons, the continuity equation is,

$$\frac{\partial n}{\partial t} + \vec{v_{e\perp}} \cdot \nabla_\perp n + n\nabla_\perp \cdot \vec{v_{e\perp}} - \frac{1}{e}\frac{\partial}{\partial z}J_z = 0, \tag{3.28}$$

substituting into Eq.(3.27) the electron velocity (Eq.(3.22)), and then considering that some terms vanish such as $\nabla_\perp \cdot \vec{v_E} = 0$, $\nabla_\perp \cdot \vec{v_{de}} = 0$ and $\vec{v_{de}} \cdot \nabla_\perp n = 0$, we obtain,

$$\left(\frac{\partial}{\partial t} + \vec{v_E} \cdot \nabla_\perp\right)n - \frac{1}{e}\frac{\partial}{\partial z}J_z = 0. \tag{3.29}$$

3.1.5 The ion continuity equation

The ion continuity equation is given by,

$$\frac{\partial n}{\partial t} + \vec{v_{i\perp}} \cdot \nabla_\perp n + n\nabla_\perp \cdot \vec{v_{i\perp}} = 0, \tag{3.30}$$

when substituting in Eq. (3.21), where $\nabla_\perp \cdot \vec{v_E} = 0$ and neglecting the non linear term $\vec{v_p}\cdot$, the equation becomes,

$$\left(\frac{\partial}{\partial t} + \vec{v_E} \cdot \nabla_\perp\right) n + n\nabla_\perp \cdot \vec{v_p} = 0. \tag{3.31}$$

Considering quasineutrality, the electron and ion continuity equations (Eqs.(3.29) and (3.31)) are equated, resulting in,

$$n\nabla_\perp \cdot \vec{v_p} = -\frac{1}{e}\frac{\partial}{\partial z} J_z. \tag{3.32}$$

The term on the left-hand side can be rewritten by substituting in Eq.(3.14),therefore, Equation (3.32) becomes,

$$\left(\frac{\partial}{\partial t} + \vec{v_E} \cdot \nabla_\perp\right) \nabla^2 \varphi = \frac{B^2}{nm_i}\frac{\partial}{\partial z} J_z, \tag{3.33}$$

where $\nabla^2 \varphi \equiv \zeta$ is the ion vorticity.

Equations 3.27, 3.29 and 3.33 form the three-dimensional HW equations. In the original HW equations, presented in the early papers by Hasegawa (Hasegawa and Wakatani, 1983) and Wakatani (Wakatani and Hasegawa, 1984), were set to describe, in a 3D system setting (Hasegawa and Wakatani, 1987), the resistive drift wave turbulence that occurs in magnetized plasma. These equations describe this phenomenon using the perturbations of plasma density (n) and electrostatic potential (φ). By eliminating J_z from equations (3.29) and (3.33) using Eq. (3.27), we obtain, respectively:

$$\left(\frac{\partial}{\partial t} + \vec{v_E} \cdot \nabla_\perp\right) n - \frac{1}{e}\frac{\partial}{\partial z}\left(\frac{T}{e\eta}\left(\frac{1}{n}\frac{\partial n}{\partial z} - \frac{e}{T}\frac{\partial \varphi}{\partial z}\right)\right) = 0, \tag{3.34}$$

$$\left(\frac{\partial}{\partial t} + \vec{v_E} \cdot \nabla_\perp\right) \nabla^2 \varphi = \frac{B^2}{nm_i}\frac{\partial}{\partial z}\left(\frac{T}{e\eta}\left(\frac{1}{n}\frac{\partial n}{\partial z} - \frac{e}{T}\frac{\partial \varphi}{\partial z}\right)\right), \tag{3.35}$$

where a coupled nonlinear equations for φ and n is constructed using the normalization (Hasegawa and Wakatani, 1983),

$$\frac{e\varphi}{T} \equiv \varphi, \qquad \omega_{ci} t \equiv t,$$
$$\frac{n_1}{n_0} \equiv n, \qquad \frac{x}{p_s} \equiv x.$$

where $p_s \equiv (T/m_i)^{1/2}/\omega_{ci}$ is the ion Larmour radius. For the purpose of this thesis, we interpret the HW coupled nonlinear equations as is written from Numata *et al.* (2007):

$$\begin{aligned}\frac{\partial}{\partial t}\zeta + \{\varphi, \zeta\} &= \alpha\,(\varphi - n) - D\nabla^4\zeta, &(3.36)\\ \frac{\partial}{\partial t}n + \{\varphi, n\} &= \alpha\,(\varphi - n) - \kappa\frac{\partial\varphi}{\partial y} - \nabla^4 n, &(3.37)\end{aligned}$$

where ζ is the ion vorticity, $\alpha = -T/(\eta n_0 \omega_{ci} e^2)\partial^2/\partial z^2$ is the adiabacity operator, and D is the dissipation coefficient. $\kappa \equiv (\partial/\ \partial x)\ln n_0$ is a constant that represents the background density. The term $\{a, b\} \equiv (\partial a/\partial x)(\partial b/\partial y) - (\partial a/\partial y)(\partial b/\partial x)$ represents the Poisson bracket. Within a Tokamak, the x and y directions are associated with the radial and poloidal directions, respectively. The importance and relevance of these parameters will be further explained in Section 3.2. The HW equations take into account the influence of non-uniform background density and the parallel motion of electrons, as defined by Ohm's law. The density gradient is responsible for driving the drift waves, which, in turn, are made unstable by the parallel electron resistivity (Numata *et al.*, 2007).

The HW equations originate from the Hasegawa-Mima equations presented in 1977 (Mima and Hasegawa, 1977) and can be reduced to two spatial dimensions (Hasegawa and Mima, 1978). In the HW equations, the α operator is responsible for making the system 3D. The α operator governs the degree to which electrons can swiftly navigate along the magnetic field lines and induce a perturbed Boltzmann density response (Anderson and Hnat, 2017). The approach taken in this thesis is turning α into a parameter to establish a 2D system setting. The values of α are presented in Section 3.2.

When the HW equations are restricted to such a setting, 2D system setting, it does not contain the zonal flow, however, Numata *et al.* (2007) presented an approach that permits the modification of the HW equations, allowing the capture of the zonal flow. This is done by subtracting the zonal components from the resistive coupling term $\alpha\,(\varphi - n)$ which turns it into $\alpha\,(\widetilde{\varphi} - \widetilde{n})$. The resistive coupling term requires careful consideration due to the fact that zonal components of fluctuations do not contribute to the parallel current. In the Tokamak edge region, any potential fluctuation on the flux surface is effectively neutralized by the parallel motion of electrons. The zonal and nonzonal components, respectively, of a variable f are defined as (Numata *et al.*, 2007):

$$\textbf{zonal}:\ \langle f\rangle = \frac{1}{L_y}\int f\,dy \tag{3.38}$$

$$\textbf{nonzonal}:\ \widetilde{f} = f -\ \langle f\rangle \tag{3.39}$$

where L_y is the length in y, and f stands for ζ and n (Numata *et al.*, 2007). The $<>$ denotes an average in the poloidal direction and $\widetilde{f}$ symbolizes the fluctuation on the flux surface averaged component removed. This yields the modified Hasegawa-Wakatani (MHW) equations presented in the next section.

3.2 MODIFIED HASEGAWA-WAKATANI EQUATIONS

The MHW equations represent a simplified model of the drift-wave turbulence in a tokamak plasma, setting it up in a 2D system setting (Numata *et al.*, 2007),

$$\begin{aligned} \frac{\partial}{\partial t}\zeta + \{\varphi, \zeta\} &= \alpha\left(\widetilde{\varphi} - \widetilde{n}\right) - D\nabla^4\zeta, && (3.40) \\ \frac{\partial}{\partial t}n + \{\varphi, n\} &= \alpha\left(\widetilde{\varphi} - \widetilde{n}\right) - \kappa\frac{\partial \varphi}{\partial y} - \nabla^4 n. && (3.41) \end{aligned}$$

In this physical configuration, the model is situated within a tokamak plasma characterized by a constant magnetic field equilibrium $\vec{B} = B_0\nabla z$, and a nonuniform density $n_0 = n_0(x)$ in the edge region. Within Equations (3.40) and (3.41), several parameters $\{a, b\}$ are utilized to represent the Poisson bracket, with n signifying the density fluctuations, and the ion vorticity $\zeta \equiv \nabla^2\varphi$ which is a 2D Laplacian ($\nabla^2 = \partial^2/\partial x^2 + \partial^2/\partial y^2$) depending on the electrostatic potential (φ). The background density $\kappa \equiv (\partial/\ \partial x)\ln n_0$ maintains an unvarying exponential profile and remains constant, while D represents the dissipation coefficient. In this physical setup, the adiabaticity operator α is assigned as a constant coefficient (Numata *et al.*, 2007). The velocity field equations are obtained from the electrostatic potential,

$$v_x \equiv -\frac{\partial \widetilde{\varphi}}{\partial y}, \tag{3.42}$$

$$v_y \equiv \frac{\partial \widetilde{\varphi}}{\partial x}. \tag{3.43}$$

The velocity field describes the instantaneous velocities of fluid elements across the studied domain. It refers to the movement of any fluid element that is currently passing through a specific area. The particle density flux Γ_r, is a correlation between the particle density (n) and radial velocity (v_r = -$\partial\widetilde{\varphi}/\ \partial y$) (Bos *et al.*, 2008),

$$\Gamma_r = \left\langle n v_r \right\rangle. \tag{3.44}$$

In this model the radial direction is represented by the x direction, therefore $v_r \equiv v_x$, whereas the poloidal direction is represented by the y direction. The MHW system, also, possesses a dynamic invariant, known as kinetic energy (E_K):

$$E_K = \frac{1}{2}m|\vec{v}|^2 = \frac{1}{2}m\left(v_x^2 + v_y^2\right) \tag{3.45}$$

where $m = 1$.

By changing the value of α and D, the MHW equations can display two different regimes, namely, a regime with turbulent patterns and formation of vortices, and a regime dominated by zonal flows (Numata *et al.*, 2007). We fix $D = 10^{-4}$ and $\kappa = 10^{-1}$, and set the α parameter to two different values, namely $\alpha = 0.0010$ and $\alpha = 0.0018$. The first value leads to numerical solutions with turbulent behavior (i.e., the low-confinement regime), whereas the second value leads to the zonal-flow regime (i.e., the high-confinement regime). We solve Eqs. (3.40)-(3.41) employing the 4th-order accuracy finite difference method with a grid resolution of 256x256 for the spatial derivatives, and the 4th-order Runge-Kutta method for time integration. The initial conditions are set to small-amplitude random fluctuations. Periodic boundary conditions are set for simplicity. The code is implemented it using a Fortran-90, and runs in parallel using the MPI protocol implemented by the MPICH library.

The 4th-order accuracy finite difference method and 4th order Runge-Kutta Method, that are implemented, are further explained in the following sections, Section 3.2.1 and Section 3.2.2, respectively.

3.2.1 4th-order Accuracy Finite Difference Method

The finite difference method is used to approximate differential equations into large algebraic systems of equations to facilitate computational calculations. The approach involves substituting the derivatives in the differential equations with finite difference approximations (LeVeque, 2005).

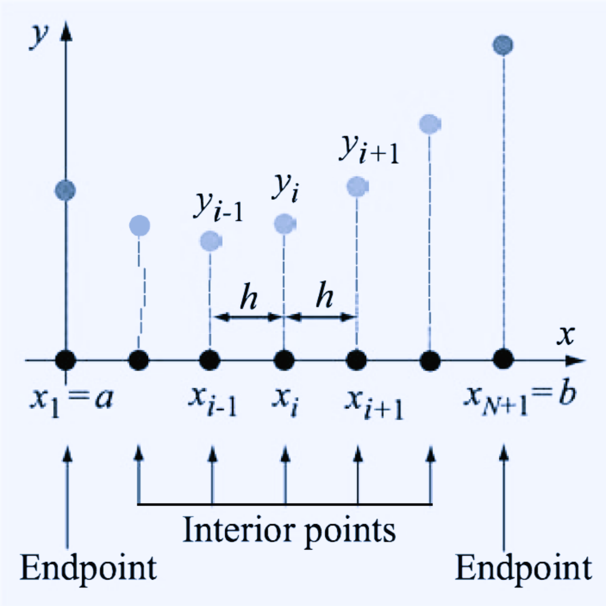

Figure 3.1. Finite Difference Method with Boundary Value Problem. Source: (Gilat and Subramaniam, 2013)

As illustrated in Fig. 3.1, the solution domain is divided into N subintervals of equal length h, defined by $(N + 1)$ points known as grid points. Each subinterval, represented as the step size, is denoted by $h = (b-a)/N$. The endpoints, a and b, are situated at the extremities, while the remaining points are interior points. At each of these interior points, we formulate the differential equation. This process yields a system of linear algebraic equations for linear differential equations or a system of nonlinear algebraic equations for nonlinear ones. Solving this system provides the numerical solution for the differential equation (Gilat and Subramaniam, 2013).

Often, finite difference methods employ central difference formulas due to their superior accuracy. Consider a function $y(x)$ provided at equally spaced points $(x_1, y_1), \ldots, (x_i, y_i), \ldots,$ (x_{N+1}, y_{N+1}) with a uniform spacing $h = x_{i+1} - x_i$ for $i = 1, \ldots, N$. The finite difference approximations of the first and second derivatives at the interior points, utilizing 4th order accuracy and central difference formulas, are expressed as (Gilat and Subramaniam, 2013):

$$\left.\frac{dy}{dx}\right|_i = \frac{y_{i+2} - 8y_{i+1} + 8y_{i-1} - y_{i-2}}{12h}, \qquad \left.\frac{d^2y}{dx^2}\right|_i = \frac{-y_{i-2} + 16y_{i-1} - 30y_i + 16y_{i+1} - y_{i+2}}{12h^2},$$

where h is the uniform spacing between adjacent points.

3.2.2 4th-order Runge-Kutta Method

Runge-Kutta methods represent a family of single-step, explicit, numerical techniques designed to solve first-order ordinary differential equations (ODEs). In the single-step approach, the solution at the following point, x_{i+1}, is derived from the known solution at the current point, x_i. Explicit methods, characteristic of Runge-Kutta techniques, employ a direct formula for computing the dependent variable's value at the next increment of the independent variable. These methods are categorized based on their "order," indicating the number of points used within a step to determine the value of coefficients. The fourth-order Runge-Kutta method requires four evaluations for each step, utilizing four points in its computation (Gilat and Subramaniam, 2013).

Runge-Kutta methods offer a more precise solution when compared to the simpler Euler's explicit method, and this precision improves (truncation error decreases) with higher orders. However, with each step, multiple evaluations of the derivative function $f(x, y)$ are required, conditional to the method's order. The predominant Runge-Kutta method in use is of order four in difference-equation form, expressed as follows (Burden and Faires, 2011):

$$y_{i+1} = y_i + \frac{1}{6}\left(K_1 + 2K_2 + 2K_3 + K_4\right)h,$$

where,

$$K_1 = f(x_i, y_i),$$

$$K_2 = f(x_i + \frac{1}{2}h, y_i + \frac{1}{2}K_1 h),$$

$$K_3 = f(x_i + \frac{1}{2}h, y_i + \frac{1}{2}K_2 h),$$

$$K_4 = f(x_i + h, y_i + K_3 h).$$

For this thesis, we solved the time integration using the values of h = 0.5 and a time step $= 5 \times 10^{-2}$.

3.3 LAGRANGIAN COHERENT STRUCTURES

The concepts situated at the intersection of nonlinear dynamics, which serves as the mathematical foundation for chaos theory and fluid dynamics, have yielded the concept of Lagrangian coherent structures (LCS). These structures offer a unique perspective on comprehending transport within intricate fluid flows. In a two-dimensional context, the LCSs manifest as material lines, which represent continuous, smooth trajectories of fluid elements transported by the flow. The LCS approach offers a mechanism for identifying crucial material lines responsible for structuring fluid-flow transport. This approach relies on identifying material lines that exhibit predominant influence in attracting and repelling neighboring fluid elements over a defined time frame. These critical lines are LCSs of the fluid flow (Peacock and Haller, 2013; Padberg *et al.*, 2007).

Two distinct viewpoints can be adopted when describing fluid flow. The Eulerian perspective involves assessing the characteristics of a flow field at specific time, while, the Lagrangian viewpoint is concerned with the identity of individual fluid elements, specifically tracking the changing velocity of individual particles along their trajectories as they are transported by the flow. The LCS approach embodies the principle of objectivity or frame invariance. Descriptions of flow structures using Eulerian field characteristics frequently lack objectivity due to their failure to remain invariant under time-dependent rotations and translations of the reference frame (Peacock and Haller, 2013; Haller and Yuan, 2000).

The ongoing challenge lies in identifying the dynamic frameworks forming material patterns in flows characterized by complex spatial and temporal structures. Typically, the flows that demand the most comprehensive understanding are usually aperiodic, with information about the associated velocity field available only in the form of observational or numerical simulation data sets over finite time intervals. Given the observation of the velocity field, the LCSs of the flow over a finite interval are the material lines that exhibit the highest local rate of repelling or attracting nearby fluid trajectories compared to other material lines in proximity. The repelling LCSs guide particles toward distinct regions compared to those influenced by the attracting LCSs (Peacock and Haller, 2013; Haller, 2011). See Figure 3.2 for a visual representation of repelling and attracting LCSs.

The identification of LCSs through the equivalence with finite-time Lyapunov exponents (FTLE) ridges presents a direct and computationally efficient approach. This method, initially introduced by Pierrehumbert and Yang (1993), offers insights into Lagrangian features within velocity-field data through plots of the FTLE field. The FTLE will be discussed further in section 3.3.1.

Another methodology, the Geodesic theory introduced by Haller and Beron-Vera (2012), provides a metric of geodesic deviation. This metric serves to establish the minimal computational time scale required for the robust numerical identification of generalized LCSs. The

Geodesic theory is presented in section 3.3.2.

3.3.1 Finite-Time Lyapunov Exponent

The FTLE represents a useful tool to analyze the chaotic mixing properties of fluids. Subsequently, we observe the resulting LCS that arise from the velocity field. These LCSs can be defined as local maxima of the FTLE fields (Haller, 2001), representing special gradient lines that are transverse to the direction of minimum curvature (Shadden *et al.*, 2005) (see Fig. 3.2).

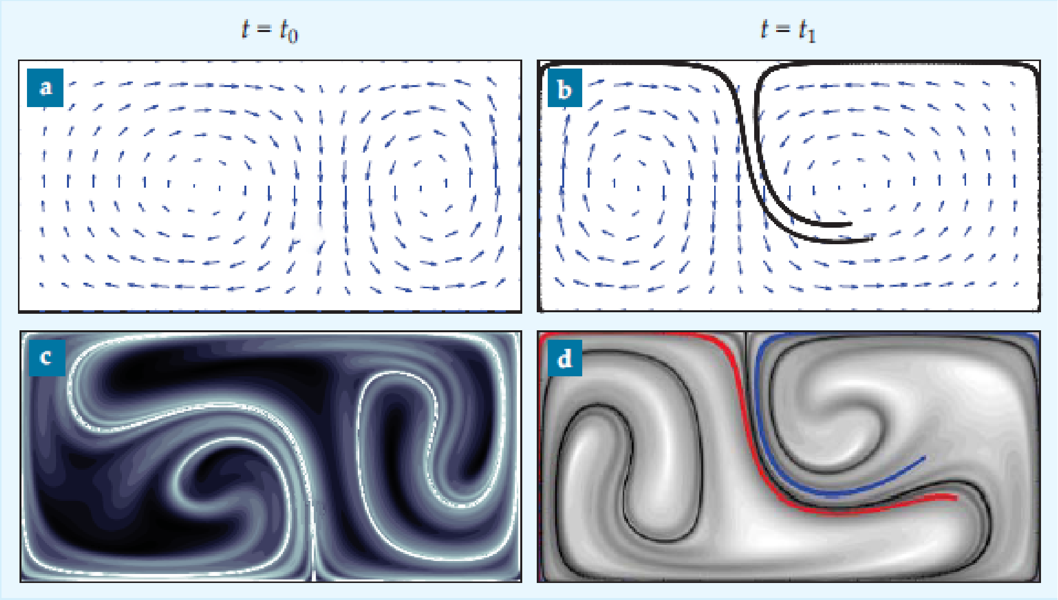

Figure 3.2. (a) The velocity field at t_0 instant is indicated by the magnitude and direction of the blue arrows. (b) Following advection by the time-dependent velocity field, the dye and the field are depicted at time t_1. (c) A candidate representing the most robust repelling LCS is delineated by the white line at time t_0. The lightest background shading corresponds to the largest positive FTLE. (d) A candidate identified as the most potent attracting LCS, illustrated by the black line at time t_1. The darkest background shading highlights the most prominent negative FTLE. Source: (Peacock and Haller, 2013)

The FTLE field is determined by the procedure that involves allowing fluid particles to evolve under the influence of the velocity field from time t_0, observing the extent of separation between initially neighboring particles at a specific location after the time τ. Regions characterized by substantial particle separation exhibit elevated FTLE values, signifying local zones where the flow experiences pronounced divergence (Peacock and Haller, 2013).

Let $D \subset \mathbb{R}^2$, and let $\vec{v}(\vec{x}, t)$ the vector field defined in D. Recall that,

$$\vec{v} = \frac{d\vec{x}}{dt}, \qquad\qquad v = |\vec{v}|.$$

The trajectory $\vec{x}(t, t_0, \vec{x_0})$ with initial condition $\vec{x}$ at time t_0 is given by,

$$\dot{\vec{x}}(t, t_0, \vec{x_0}) = \vec{v}(\vec{x}(t, t_0, \vec{x_0}), t), \tag{3.46}$$

where the dot represents d/dt . The solution to Eq. (3.46) can be viewed as a mapping process, referred as the flow map, denoted by $\phi_{t_0}^{t_0+\tau}$:

$$\phi_{t_0}^{t_0+\tau}: \begin{cases} D & \longrightarrow D \\ \vec{x} & \longrightarrow \phi_{t_0}^{t_0+\tau} = \vec{x}(t, t_0, \vec{x_0}) \end{cases} \tag{3.47}$$

The FTLE is defined as a finite time average of the maximum expansion rate for a pair of particles that are advected in the flow (Shadden *et al.*, 2005). Another definition characterizes the Lyapunov exponent as a measure of the sensitivity of a fluid particle's future behavior (Peacock and Haller, 2013). To define the FTLE mathematically, we must first consider the evolution of a perturbed point $\vec{x}' = \vec{x} + \delta\vec{x}$, where $\delta\vec{x}$ is infinitesimal and arbitrarily oriented. After an interval τ, this perturbation becomes,

$$\begin{aligned} \delta\vec{x} &= \vec{x}' - \vec{x}, \\ \delta\vec{x}_\tau &= \phi_{t_0}^{t_0+\tau}\left(\vec{x}'\right) - \phi_{t_0}^{t_0+\tau}\left(\vec{x}\right). \end{aligned} \tag{3.48}$$

Recall that, for a given function f, evaluated at a given position x, one can write the Taylor expansion around $x = a$,

$$f(x)|_a = f(a) + \frac{1}{1!}\frac{df(a)}{dx}(x-a) + \frac{1}{2!}\frac{df(a)}{dx}(x-a)^2$$

where the flow map is denoted as $\phi_{t_0}^{t_0+\tau}$, a map which takes a point in the domain at time t_0 to its location at time $t_0 + \tau$, and can be expanded into a Taylor series in the neighborhood of $\vec{x}$,

$$\begin{aligned} \phi_{t_0}^{t_0+\tau}\left(\vec{x}'\right)\Big|_{\vec{x}} &= \phi_{t_0}^{t_0+\tau}\left(\vec{x}\right) + \left.\frac{d\phi_{t_0}^{t_0+\tau}}{d\vec{x}}\right|_{\vec{x}}\left(\vec{x}' - \vec{x}\right) + \dots \\ &\approx \phi_{t_0}^{t_0+\tau}\left(\vec{x}\right) + \left.\frac{d\phi_{t_0}^{t_0+\tau}}{d\vec{x}}\right|_{\vec{x}}\left(\vec{x}' - \vec{x}\right), \end{aligned} \tag{3.49}$$

where,

$$\frac{d\phi_{t_0}^{t_0+\tau}}{d\vec{x}} = \frac{d\vec{x}(t+\tau, t_0, \vec{x_0})}{d\vec{x}} = \begin{bmatrix} \frac{\partial x}{\partial x_0} & \frac{\partial x}{\partial y_0} \\ \frac{\partial y}{\partial x_0} & \frac{\partial y}{\partial y_0} \end{bmatrix}.$$

Substituting Equations (3.49) into (3.48) we obtain:

$$\delta\vec{x}_\tau = \phi_{t_0}^{t_0+\tau}\left(\vec{x}\right) + \left.\frac{d\phi_{t_0}^{t_0+\tau}}{d\vec{x}}\right|_{\vec{x}}\delta\vec{x}_0 - \phi_{t_0}^{t_0+\tau}\left(\vec{x}\right) = \left.\frac{d\phi_{t_0}^{t_0+\tau}}{d\vec{x}}\right|_{\vec{x}}\delta\vec{x}_0. \tag{3.50}$$

The growth of the infinitesimal perturbation, also obtained by applying the modules of $\delta\vec{x}_\tau$, will be given by;

$$\begin{aligned}\|\delta\vec{x}_\tau\| &= \| \left.\frac{d\phi_{t_0}^{t_0+\tau}}{d\vec{x}}\right|_{\vec{x}} \delta\vec{x}_0 \| = \| \frac{d\phi_{t_0}^{t_0+\tau}(\vec{x})}{d\vec{x}} \delta\vec{x}_0 \| \\ &= \sqrt{\left(\frac{d\phi_{t_0}^{t_0+\tau}(\vec{x})}{d\vec{x}}\delta\vec{x}_0\right)\cdot\left(\frac{d\phi_{t_0}^{t_0+\tau}(\vec{x})}{d\vec{x}}\delta\vec{x}_0)\right)}. \end{aligned} \tag{3.51}$$

By applying the identity,

$$(A\vec{v})\cdot(A\vec{v}) = \vec{v}\cdot\left(A^T A\vec{v}\right)$$

we obtain the initial perturbation:

$$\|\delta\vec{x}_\tau\| = \sqrt{\delta\vec{x}_0\cdot\left[\left(\frac{d\phi_{t_0}^{t_0+\tau}(\vec{x})}{d\vec{x}}\right)^T\left(\frac{d\phi_{t_0}^{t_0+\tau}(\vec{x})}{d\vec{x}}\right)\delta\vec{x}_0\right]} \tag{3.52}$$

The Cauchy-Green tensor, in a 2D fluid flow, is a positive-definite 2 x 2 symmetric matrix computed for every initial position within the fluid (Peacock and Haller, 2013). Let us define a finite-time version of the right Cauchy-Green deformation tensor as:

$$C_{t_0}^{t_0+\tau} = \left(\frac{d\phi_{t_0}^{t_0+\tau}(\vec{x})}{d\vec{x}}\right)^T\left[\frac{d\phi_{t_0}^{t_0+\tau}(\vec{x})}{d\vec{x}}\right], \tag{3.53}$$

and denote the eigenvectors of $C_{t_0}^{t_0+\tau}$ as $\vec{\xi}_1$ and $\vec{\xi}_2$, with corresponding eigenvalues $\lambda_1 > \lambda_2$ satisfying,

$$C_{t_0}^{t_0+\tau}\vec{\xi}_i = \lambda_i\vec{\xi}_i,\ i = 1,\ 2, \tag{3.54}$$

and $\left\|\vec{\xi}_i\right\| = 1$. In addition, if we assume that the perturbation $\delta\vec{x}$ is aligned with the direction of maximum stretching $\vec{\xi}_1$, then we can write:

$$\delta\vec{x}_0 = \|\delta\vec{x}_0\|\ \vec{\xi}_1. \tag{3.55}$$

Inserting Equation (3.55) into (3.52), we obtain:

$$\|\delta\vec{x}_\tau\| = \sqrt{\|\delta\vec{x}_0\|^2 \ \vec{\xi}_1 \cdot \left[\left(\frac{d\phi_{t_0}^{t_0+\tau}(\vec{x})}{d\vec{x}} \right)^T \left(\frac{d\phi_{t_0}^{t_0+\tau}(\vec{x})}{d\vec{x}} \right) \vec{\xi}_1 \right]}. \tag{3.56}$$

Substituting Equation (3.53) into (3.56),

$$\|\delta\vec{x}_\tau\| \approx \sqrt{\|\delta\vec{x}_0\|^2 \ \vec{\xi}_1 \cdot C_{t_0}^{t_0+\tau}\vec{\xi}_1}. \tag{3.57}$$

then using Eq.(3.54), we obtain:

$$\|\delta\vec{x}_\tau\| \approx \sqrt{\|\delta\vec{x}_0\|^2 \ \vec{\xi}_1 \cdot \left(\lambda_i\vec{\xi}_1\right)} = \|\delta\vec{x}_0\| \sqrt{\lambda_i\vec{\xi}_1 \cdot \ \vec{\xi}_1}$$

$$\|\delta\vec{x}_\tau\| = \sqrt{\lambda_1} \ \|\delta\vec{x}_0\|. \tag{3.58}$$

Finally, the definition of the FTLE can be derived from Eq. (3.58) (Shadden *et al.*, 2005), where Eq. (3.58) can be written as,

$$\|\delta\vec{x}_\tau\| \approx e^{\sigma_{t_0}^{t_0+\tau}(\vec{x})|\tau|} \ \|\delta\vec{x}_0\|,$$

resulting in:

$$\sigma_{t_0}^{t_0+\tau}(\vec{x}) = \frac{1}{|\tau|} \ln \sqrt{\lambda_1}, \tag{3.59}$$

where the largest/maxima FTLE is given by Eq. (3.59) and can be computed for both positive and negative integration times (τ) due to the absolute value operation. The positive integration time is a forward-time integration that reveals a repelling LCS (Haller, 2001; Shadden *et al.*, 2005; Lekien *et al.*, 2007). Note that the spatial dependence of $\sigma_{t_0}^{t_0+\tau}$ is implicit on λ_1.

The FTLE is computed with a grid resolution of 1024x1024 and 2048x2048, and the results obtained are visualized and analyzed using Matlab, we also compute probability distribution functions (PDFs) of FTLE values with Matlab.

3.3.2 Geodesic Theory

The Geodesic theory functions as a systematic approach for identifying essential material transport barriers within two-dimensional non-autonomous dynamical systems (Haller and Beron-Vera, 2012). This methodology involves the characterization of transport barriers as exceptional material lines exhibiting minimal deformation compared to their neighboring lines. The primary goal is to identify the material lines with the least stretching locally in forward or backward time. This theoretical framework represents an extension of the concept of LCSs from hyperbolic material lines (Haller, 2011) to encompass elliptic and parabolic material lines. It is set in temporally aperiodic flows defined over finite time intervals (Haller and Beron-Vera, 2012).

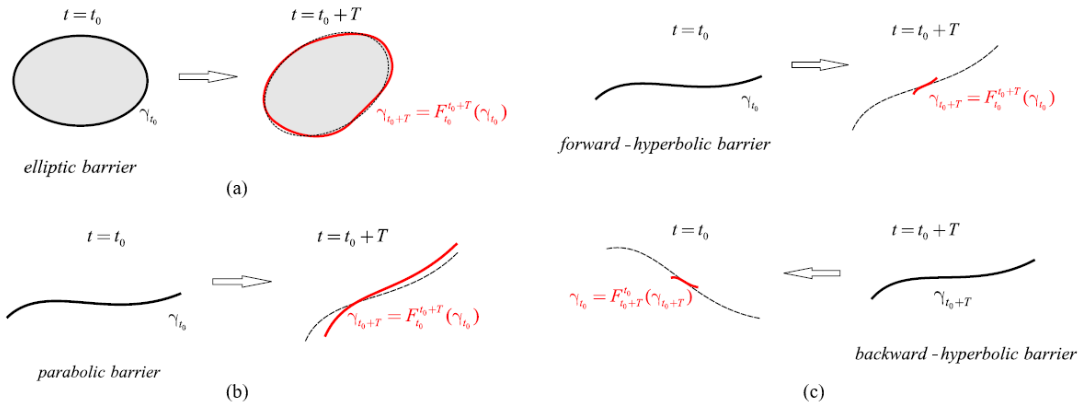

Figure 3.3. (a) Diagram illustrating an elliptic transport barrier. It features a closed shearline where the advected material γ_{t_0+T} possesses the same arclength and encloses the same area as γ_{t_0}. (b) Diagram depicting a parabolic transport barrier. It includes an open shearline where the advected material γ_{t_0+T} has the same arclength as γ_{t_0}. (c) Diagram illustrating forward- and backward-hyperbolic transport barriers. These involve strainlines where the arclength of γ_{t_0+T} and γ_{t_0} shrinks exponentially under forward-time and backward-time advection, respectively, as governed by the flow map. Source: (Haller and Beron-Vera, 2012)

This approach leads to trajectories of ODEs for forward- and backward-time hyperbolic and shear transport barriers. The trajectories they describe are snapshots of instant frozen-in-time influential material lines in the phase space. These influential material lines, termed as strainlines and shearlines, act as strong transport barriers, particularly when closely aligned with least-stretching geodesics derived from the metric induced by the Cauchy-Green strain tensor(Haller and Beron-Vera, 2012). Strainlines are curves tangent to the eigenvector field of the Cauchy-Green strain tensor computed over a specific time window (Peacock and Haller, 2013). Strainlines that are more locally repelling than their neighbors are identified as hyperbolic LCSs (Farazmand and Haller, 2012). Shearlines are further categorized into closed and open shearlines, with closed shearlines representing elliptic barriers in incompressible, finite-time, non-autonomous dynamical systems on the plane. These elliptic barriers play a role as generalized Lagrangian eddy barriers. On the other hand, open shearlines are conceptualized as frame-independent extensions of non-stretching streamlines forming steady shear jets, referred to as parabolic barriers (Haller and Beron-Vera, 2012). See Figure 3.3 for a visual representation of hyperbolic, elliptic and parabolic barriers.

The Cauchy-Green metric functions operate within the spatial domain of initial fluid particle positions, wherein strainlines and shearlines delineate the initial locations of transport barriers. Proximity to the least-stretching geodesics is measured through the geodesic deviation, representing the pointwise C^2 - distance between a curve and the most shrinking Cauchy-Green geodesic passing through the same point. The analysis of transport barriers involves the integration of trajectories, which can be concluded when the geodesic deviation on strainlines and shearlines falls below a specified error threshold (Haller and Beron-Vera, 2012).

The next sections are focused on defining the Lagrangian shear and its locally maximal directions, to further our understanding of the Geodesic Theory. The maximized Lagrangian shear permits the boundary condition for the identification of shear transport barriers, which is the main focus of this thesis when utilizing the geodesic method.

3.3.2.1 Definition of Lagrangian shear

Let $M(t)$ be an evolving material line. At a point $\vec{x}_0 \in M(t)$, a unit n_0 to $M(t)$ can be written as,

$$\vec{n}_0 = \Omega \vec{e}_0 \tag{3.60}$$

where,

$$\Omega = \begin{bmatrix} 0 & -1 \\ 1 & 0 \end{bmatrix},$$

and $\vec{e}_0 \in T_{x_0}M(t)$ is a unit tangent vector. Due to the invariance of the flow map, the tangent space is carried forward by the linearized flow map, as defined by Haller and Beron-Vera (2012) as $\nabla F_{t_0}^t(\vec{x_0})$, into the tangent space,

$$T_{\vec{x}_t}M(t) = \nabla F_{t_0}^t(\vec{x_0}) T_{\vec{x}_0} M(t_0),$$

where (Peacock and Haller, 2013),

$$F_{t_0}^t(x_0) = x\left(t, t_0, x_0\right), \qquad \nabla F_{t_0}^t(x_0) = \begin{bmatrix} \frac{\partial x}{\partial x_0} & \frac{\partial x}{\partial y_0} \\ \frac{\partial y}{\partial x_0} & \frac{\partial y}{\partial y_0} \end{bmatrix}.$$

Therefore a unit tangent vector in $T_{\vec{x}_t}M(t)$ can be selected as,

$$\vec{e}_t = \frac{\nabla F_{t_0}^t(\vec{x_0})\vec{e}_0}{|\nabla F_{t_0}^t(\vec{x_0})\vec{e}_0|}. \tag{3.61}$$

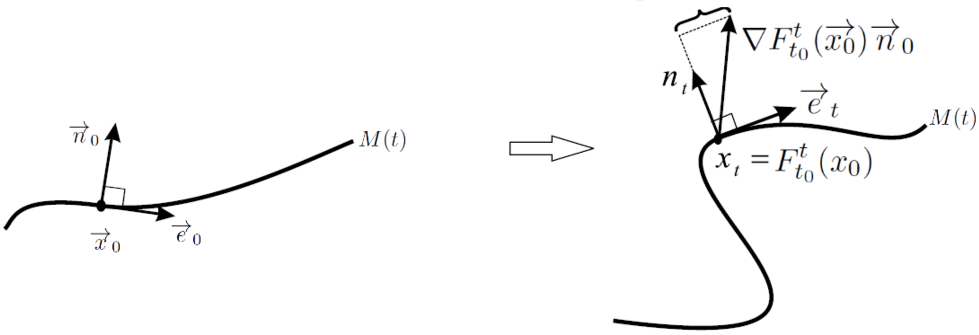

Figure 3.4. The definition of the Lagrangian shear $\sigma_{t_0}^t$. Source: (Haller and Beron-Vera, 2012)

Let us define the Lagrangian shear $\sigma_{t_0}^t$ as the normal projection of the linearly advected unit normal $\nabla F_{t_0}^t(\vec{x_0})\vec{n}_0$ onto the advected unit tangent $\vec{e}_t$ (Haller and Beron-Vera, 2012), as shown in Fig.3.4, and can be computed as:

$$\sigma_{t_0}^t(\vec{x_0}, \vec{e}_0) = \left\langle \vec{e}_t, \nabla F_{t_0}^t(\vec{x_0})\vec{n}_0 \right\rangle . \tag{3.62}$$

By substituting Equations (3.61) into (3.62), and applying the identity $\langle A\vec{u}, A\vec{v}\rangle = \left\langle \vec{u}, A^T A\vec{v}\right\rangle$ we obtain:

$$\sigma_{t_0}^t(\vec{x_0}, \vec{e}_0) = \frac{1}{|\nabla F_{t_0}^t(\vec{x_0})\vec{e}_0|} \left\langle \Omega\vec{e}_t, \left(\nabla F_{t_0}^t(\vec{x_0})\right)^T \left(\nabla F_{t_0}^t(\vec{x_0})\right) \vec{e}_0 \right\rangle . \tag{3.63}$$

The Cauchy-Green strain tensor is formally identified as a classical positive definite tensor field employed for characterizing the deformation of moving continua (Truesdell *et al.*, 2004; Ottino, 1989). Defining the Cauchy-Green strain tensor as $C_{t_0}^t(\vec{x_0}) = \left(\nabla F_{t_0}^t(\vec{x_0})\right)^T \left(\nabla F_{t_0}^t(\vec{x_0})\right)$ and substituting into Eq. (3.63) and simplifying, we obtain:

$$\sigma_{t_0}^t(\vec{x_0}, \vec{e}_0) = \frac{1}{|\nabla F_{t_0}^t(\vec{x_0})\vec{e}_0|} \left\langle \Omega\vec{e}_t, C_{t_0}^t(\vec{x_0})\vec{e}_0 \right\rangle = \frac{1}{\sqrt{\left\langle \vec{e}_t, C_{t_0}^t(\vec{x_0})\vec{e}_0 \right\rangle}} \left\langle \Omega\vec{e}_t, C_{t_0}^t(\vec{x_0})\vec{e}_0 \right\rangle . \tag{3.64}$$

3.3.2.2 Directions and magnitude of maximal Lagrangian shear

We write the tangent vector $\vec{e}_0$ as a linear combination of eigenvectors $\vec{\xi}_1$ and $\vec{\xi}_2$:

$$\begin{cases} \vec{e}_0 = \alpha\vec{\xi}_1 + \beta\vec{\xi}_2 \\ \alpha^2 + \beta^2 = 1 \end{cases} \tag{3.65}$$

where $\alpha = \alpha(x)$ and $\beta = \beta(x)$ are constants yet to be determined. Substituting Equations (3.65) into (3.64) we obtain:

$$\sigma_{t_0}^t(\vec{x_0}, \alpha, \beta) = \frac{1}{\sqrt{\left\langle \alpha\vec{\xi}_1 + \beta\vec{\xi}_2, C_{t_0}^t(\vec{x_0})(\alpha\vec{\xi}_1 + \beta\vec{\xi}_2) \right\rangle}} \left\langle \Omega(\alpha\vec{\xi}_1 + \beta\vec{\xi}_2), C_{t_0}^t(\vec{x_0})(\alpha\vec{\xi}_1 + \beta\vec{\xi}_2) \right\rangle . \tag{3.66}$$

The terms $\left\langle \alpha\vec{\xi}_1 + \beta\vec{\xi}_2, C_{t_0}^t(\vec{x_0})(\alpha\vec{\xi}_1 + \beta\vec{\xi}_2) \right\rangle = \alpha^2\lambda_1 + \beta^2\lambda_2$ and (...)
$\left\langle \Omega(\alpha\vec{\xi}_1 + \beta\vec{\xi}_2), C_{t_0}^t(\vec{x_0})(\alpha\vec{\xi}_1 + \beta\vec{\xi}_2) \right\rangle = \alpha\beta(\lambda_2 - \lambda_1)$, where λ_1 and λ_2 are corresponding eigenvalues. Substituting these terms into Eq. (3.66), we obtain:

$$\sigma_{t_0}^t(\vec{x_0},\alpha,\beta) = \frac{1}{\sqrt{\alpha^2\lambda_1+\beta^2\lambda_2}}\cdot\alpha\beta(\lambda_2-\lambda_1) = \frac{\alpha\beta(\lambda_2-\lambda_1)}{(\alpha^2\lambda_1+\beta^2\lambda_2)^{1/2}}. \tag{3.67}$$

Since we are seeking extrema of $\sigma_{t_0}^t(\vec{x_0},\alpha,\beta)$ with the constant $\alpha^2+\beta^2=1$, we can apply the method of Lagrange multipliers.

The method of Lagrange multipliers allows to find local maxima and minima of a function with constraints. For example, let f and g be functions with first partial derivatives. The Lagrange function is defined by:

$$\mathcal{L}(x,y,\lambda) = f(x,y) - \lambda g(x,y),$$

λ is the Lagrange multiplier. Local extremas are given by:

$$\nabla_{x,y,\lambda}\mathcal{L}(x,y,\lambda) = 0,$$

where $\nabla_{x,y,\lambda} = (\partial/\partial x, \partial/\partial y, \partial/\partial\lambda)$. Applying this method to the Lagrangian shear $\sigma_{t_0}^t(\vec{x_0},\alpha,\beta)$, we have that:

$$\mathcal{L}(x,y,\lambda) = \sigma_{t_0}^t(\vec{x_0},\alpha,\beta) - \lambda(\alpha^2+\beta^2-1) = \frac{\alpha\beta(\lambda_2-\lambda_1)}{(\alpha^2\lambda_1+\beta^2\lambda_2)^{1/2}} - \lambda(\alpha^2+\beta^2-1). \tag{3.68}$$

Next, we write Eq. (3.68) in terms of each component of the gradient of the Lagrange function,

$$\nabla_{\alpha,\beta,\lambda}\mathcal{L}(\alpha,\beta,\lambda) = 0.$$

The first component gives:

$$\frac{\partial}{\partial\alpha}\left\{\frac{\alpha\beta(\lambda_2-\lambda_1)}{(\alpha^2\lambda_1+\beta^2\lambda_2)^{1/2}} - \lambda(\alpha^2+\beta^2-1)\right\} = 0 \Rightarrow \frac{\beta^3\lambda_2(\lambda_2-\lambda_1)}{(\alpha^2\lambda_1+\beta^2\lambda_2)^{3/2}} - 2\lambda\alpha = 0. \tag{3.69}$$

The second component gives:

$$\frac{\partial}{\partial\beta}\left\{\frac{\alpha\beta(\lambda_2-\lambda_1)}{(\alpha^2\lambda_1+\beta^2\lambda_2)^{1/2}} - \lambda(\alpha^2+\beta^2-1)\right\} = 0 \Rightarrow \frac{\alpha^3\lambda_2(\lambda_2-\lambda_1)}{(\alpha^2\lambda_1+\beta^2\lambda_2)^{3/2}} - 2\lambda\beta = 0. \tag{3.70}$$

The third and last component gives:

$$\frac{\partial}{\partial \lambda}\left\{\frac{\alpha\beta(\lambda_2-\lambda_1)}{(\alpha^2\lambda_1+\beta^2\lambda_2)^{1/2}}-\lambda(\alpha^2+\beta^2-1)\right\}=0 \Rightarrow -\frac{\partial}{\partial \lambda}\left\{\lambda(\alpha^2+\beta^2-1)\right\}=0 \Rightarrow \alpha^2+\beta^2-1=0,$$

which is the constraint itself $\alpha^2+\beta^2=1$.

When combining Equations (3.69) and (3.70) it yields $\frac{\alpha}{\beta}=\pm\sqrt[4]{\frac{\lambda_2}{\lambda_1}}$. Solving for α and β, and then substituting into the constraint itself $\alpha^2+\beta^2=1$, it gives:

$$\alpha=\pm\sqrt{\frac{\sqrt{\lambda_2}}{\sqrt{\lambda_1}+\sqrt{\lambda_2}}}, \qquad \beta=\pm\sqrt{\frac{\sqrt{\lambda_1}}{\sqrt{\lambda_1}+\sqrt{\lambda_2}}}. \tag{3.71}$$

Substituting into Equation (3.65) the values in (3.71), we can finally write the tangent vectors that maximize the Lagrangian shear as:

$$\vec{\eta_\pm}=\sqrt{\frac{\sqrt{\lambda_2}}{\sqrt{\lambda_1}+\sqrt{\lambda_2}}}\vec{\xi_1}\pm\sqrt{\frac{\sqrt{\lambda_1}}{\sqrt{\lambda_1}+\sqrt{\lambda_2}}}\vec{\xi_2}.$$

Note that $\vec{\eta_+}$ gives the same result as $\vec{\eta_-}$. Substituting these vectors into Eq.3.64 it gives the extremum values (Haller and Beron-Vera, 2012),

$$\sigma_{t_0}^{t}(\vec{x},\eta_\pm(\vec{x}))=\pm\frac{\sqrt{\lambda_2(\vec{x})}-\sqrt{\lambda_1(\vec{x})}}{\sqrt[4]{\lambda_1(\vec{x})\lambda_2(\vec{x})}}, \tag{3.72}$$

which means that $\sigma_{t_0}^{t}$ will be maximum along the vectors ($\vec{\eta_\pm}$). Therefore, the values in Eq. 3.72 represent locally maximal positive and negative Lagragian shear values (Haller and Beron-Vera, 2012).

The Geodesic theory's Lagrangian shearlines is computed with a grid resolution of 1024x1024, and the results obtained are visualized and analyzed using GNUPLOT and MATLAB.

4 SIMULATION RESULTS AND DISCUSSIONS

4.1 MODIFIED HASEGAWA-WAKATANI EQUATIONS

A transition from L-H regimes in tokamaks can be modeled by varying the control parameter α in Eqs. (3.40)-(3.41). This transition can provide insight into the behavior of tokamak plasmas under different confinement conditions. Figure 4.1 depicts the 2D spatial patterns of the electrostatic potential φ obtained from numerical solutions of Eqs. (3.40)-(3.41) in two different regimes. The left panel of Figure 4.1 displays the patterns of φ in the turbulent regime, whereas the right panel of Figure 4.1 shows the patterns of φ in the zonal flow regime. The patterns were obtained by setting the value of the adiabaticity parameter α = 0.010 (turbulent regime) and α = 0.018 (zonal flow regime). Note that the color bars are set to the same scale, to facilitate the comparison between regimes. In this model, the left panel represents L-mode, while the right panel represents H-mode.

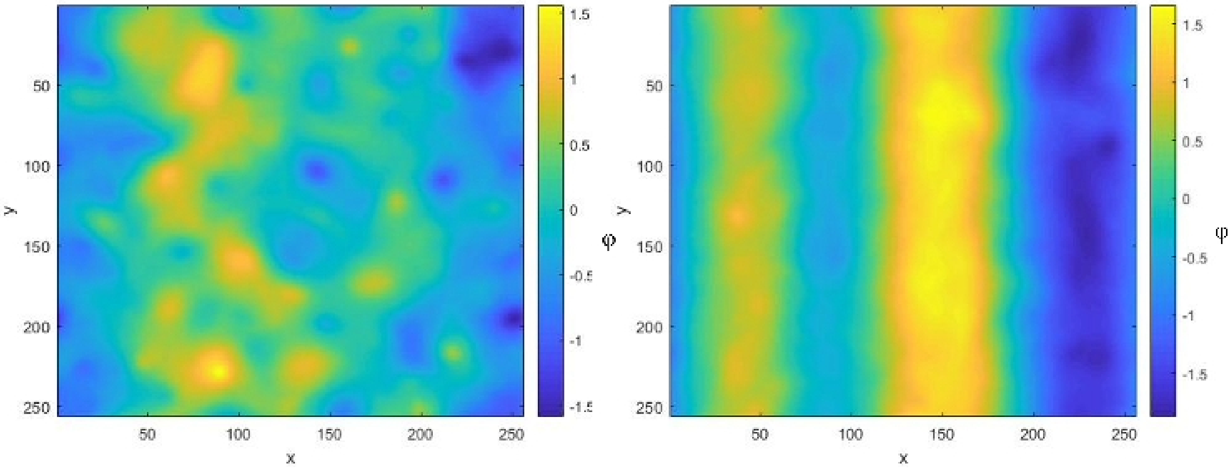

Figure 4.1. The electrostatic potential in the turbulent regime (left panel, α = 0.010) and zonal flow (right panel, α = 0.018).

The right-hand side of Fig. 4.1 shows that φ displays zonally elongated structures visible as large-scale structures in the Y direction. These structures correspond to the zonal flows that emerge as a consequence of the KH instability of the drift waves, which effectively dampens drift wave activity (Numata *et al.*, 2007). Consequently, the zonal flow exhibits high confinement properties, rendering it a crucial element in comprehending plasma turbulence and confinement in tokamaks. Conversely, in the turbulent regime (left-hand side of Fig. 4.1), φ displays a disordered pattern, which enhances drift wave activity and particle flow in the radial direction (i.e., the horizontal direction).

Table 4.1. Numerical values of Γ_r for the two regimes

Turbulent regime	0.0132
Zonal flow	0.0029

Following Bos *et al.* (2008), we calculate the particle density flux Γ_r (Eq. (3.44)) of the turbulent and zonal flow regimes across the entire simulation domain. The computed values are shown in Table 4.1. These results show that the turbulent regime displays a higher Γ_r value compared to the zonal flow regime. This is expected since the elongated patterns of the zonal flow act as transport barriers for the flow. This result emphasizes the importance of controlling turbulent flows for the confinement of plasma in a Tokamak.

Table 4.2. Numerical values of E_K for the two regimes

Turbulent regime	0.0352
Zonal flow	0.0831

In accordance with Numata *et al.* (2007), we calculate the kinetic energy E_K (Eq. (3.45)) for both turbulent and zonal flow regimes spanning the entire simulation domain. The calculated values are outlined in Table 4.2. The findings indicate that the zonal flow exhibits a notably higher E_K value in comparison to the turbulent regime. This outcome is anticipated, as the zonal flow acts as a carrier of kinetic energy absorbed from the energy of drift waves (Numata *et al.*, 2007).

Patterns of φ such as those shown in Figure 4.1 can offer clues about the presence of coherent structures. For instance, vortices can be associated with areas of localized minima and maxima of φ. These areas are readily discernible in the turbulent regime. Nonetheless, employing snapshots of fields (i.e., an Eulerian approach) for the detection of coherent structures such as vortices can yield misleading outcomes (Peacock and Haller, 2013). Coherent structures can be objectively identified using a Lagrangian approach, which will be applied in the next section.

4.2 FINITE-TIME LYAPUNOV EXPONENT

Figure 4.2 depicts the FTLE field ($\sigma_{t_0}^{t_0+\tau}$) obtained from the time-dependent velocity fields in the turbulent and the zonal flow regimes. The FTLE field was computed by setting $t_0 = 0$ and $\tau = 40\ \Omega_{ci}^{-1}$, where Ω_{ci} represent the ion cyclotron frequency, which is a fundamental time scale in plasmas. The value of τ must be obtained after some trial-and-error, checking the convergence of patterns of the FTLE field (Miranda *et al.*, 2013). Figure 4.2 offers a more detailed understanding of the spatiotemporal patterns of both the turbulent regime and the zonal flow regimes, for example, the locations of transport barriers within the flow. The numerical values of ($\sigma_{t_0}^{t_0+\tau}$) are represented using a color gradient, and fluid barriers can be identified in yellow. It becomes evident when comparing both panels of Figure 4.2 that these barriers seem to highlight locations of vortex structures in the turbulent regime (left panel), whereas in the zonal-flow regime, there seems to be a fewer number of vortices.

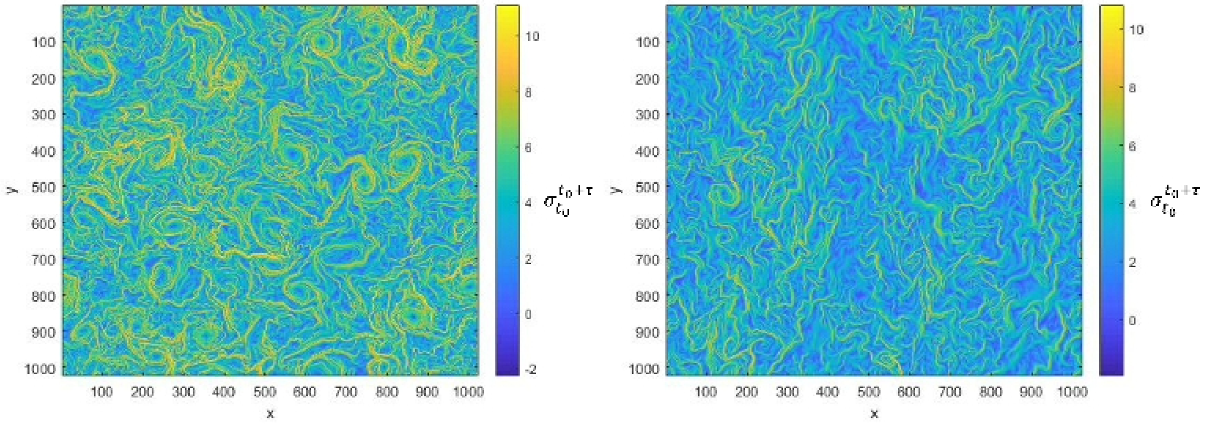

Figure 4.2. The FTLE in the turbulent regime (left panel) and zonal flow (right panel).

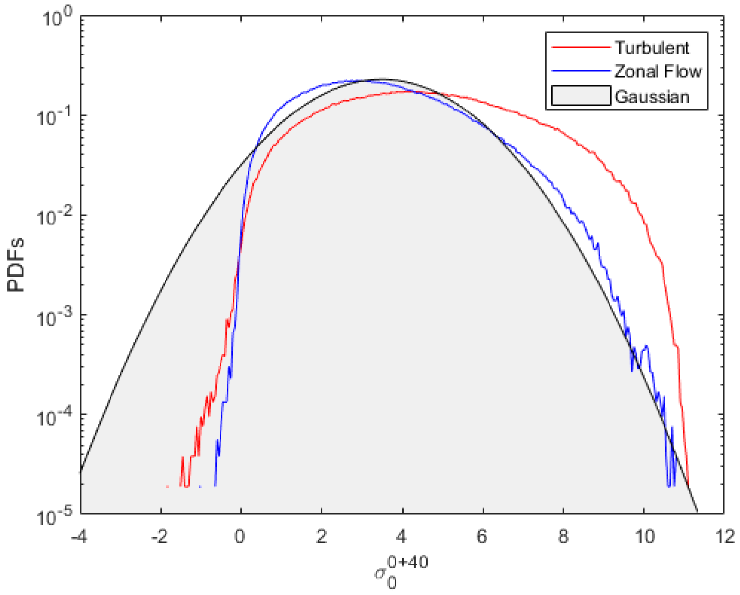

Figure 4.3. PDFs of FTLE in the turbulent regime (red line) and the zonal flow regime (blue line).

The FTLE field provides a clear identification of coherent structures such as vortices, compared to an analysis based on an instantaneous snapshot such as those shown in Fig. 4.1. For example, a comparison between Figures 4.1 and 4.2 reveals that not every localized maximum or minimum of φ from Figure 4.1 corresponds to a vortex. Moreover, the definition of vortex boundaries using instantaneous φ patterns can be a difficult task, and it is not certain that Eulerian vortices have a long duration. Lagrangian techniques such as the FTLE field allow to distinguish vortex boundaries by ridges of the FTLE field. This observation suggests that the FTLE is more effective at detecting vortices when compared to a visual inspection of the electrostatic potential.

The chaotic mixing properties of flows can be characterized from statistics of the FTLE field ($\sigma_{t_0}^{t_0+\tau}$). For example, the presence of broad PDFs can be linked to heterogeneous mixing (Beron-Vera *et al.*, 2010; Miranda *et al.*, 2013). The PDFs of the FTLE field depicted in Fig. 4.2, are presented in Fig. 4.3. Note the incorporation of a Gaussian distribution in the background of Fig.4.3, strategically employed to accentuate the asymmetry inherent in the PDFs. From this figure, the PDF of the turbulent regime displays a broader shape compared to the PDF of the zonal flow regime. This result reveals that the turbulent regime exhibits a more heterogeneous mixing pattern than the zonal flow regime. The difference in mixing can be attributed to the fact that the zonal flow is a regime of high confinement that suppresses turbulent transport (Numata *et al.*, 2007), whereas the turbulent regime is characterized by the presence of vortices that propagate across the simulation domain, trapping plasma particles and transporting them in different directions, including the positive X direction, which in this model represents the radial direction towards the walls. Therefore, the PDFs displayed in Fig.4.3 represent an alternative technique to quantify chaotic mixing in turbulent flows.

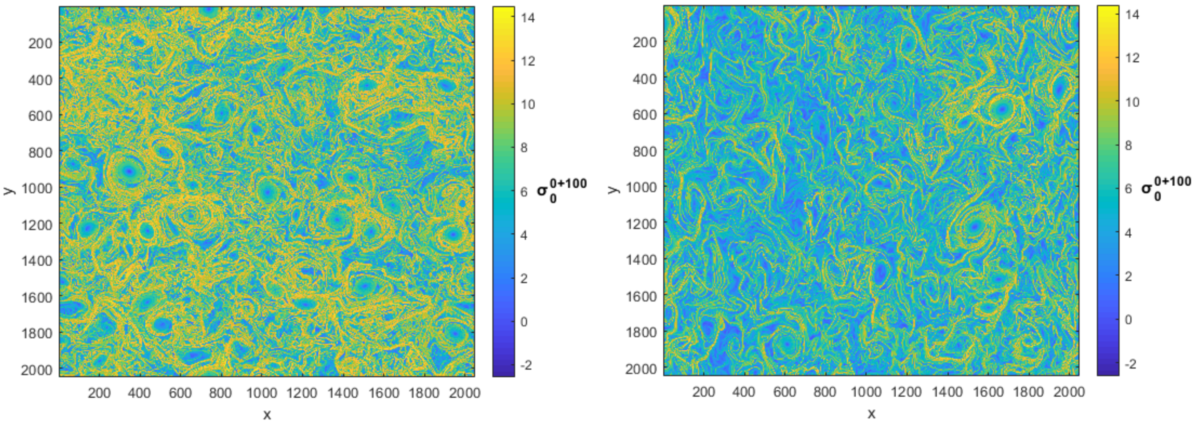

Figure 4.4. The FTLE in the turbulent regime (left panel) and zonal flow (right panel) from $t = 0$ to $t = 100$ for $\tau = 100\ \Omega_{ci}^{-1}$.

We extended our investigation of the FTLE by computing it from $t = 0$ to $t = 500$ using a time step of $\tau = 100\ \Omega_{ci}^{-1}$, necessitating a higher grid resolution of 2048x2048. The figures and their corresponding PDFs are presented as follows. Figure 4.4 follows a similar format as Fig. 4.2, offering a side-by-side comparison of the turbulent regime and the zonal flow. However, Figure 4.4 illustrates the evolution of the two regimes over a more extended period with $\tau = 100\Omega_{ci}^{-1}$. Allowing for this extension, we observed a more pronounced formation of transport barriers, aligning with our expectations. Nevertheless, the previously drawn conclusions from Fig. 4.2 remain valid. The turbulent regime still exhibits a higher prevalence of stronger transport barriers and the potential formation of vortices. Figures 4.7 and 4.8 depict the evolution of the turbulent regime and zonal flow for $t = 100$ to $t = 500$, respectively. Similar conclusions can be drawn about them as well. Their respective PDFs for times $t = 0$ to $t = 500$ are shown in Figures 4.5 and 4.6. Observation of asymmetry is evident across all PDFs depicted in Figures 4.5 and 4.6

We computed the variance for each PDFs curve from $t = 0$ to $t = 500$ for $\tau = 100\ \Omega_{ci}^{-1}$ for each regime, and the results are presented in Tab.4.3. Calculating the variance provides

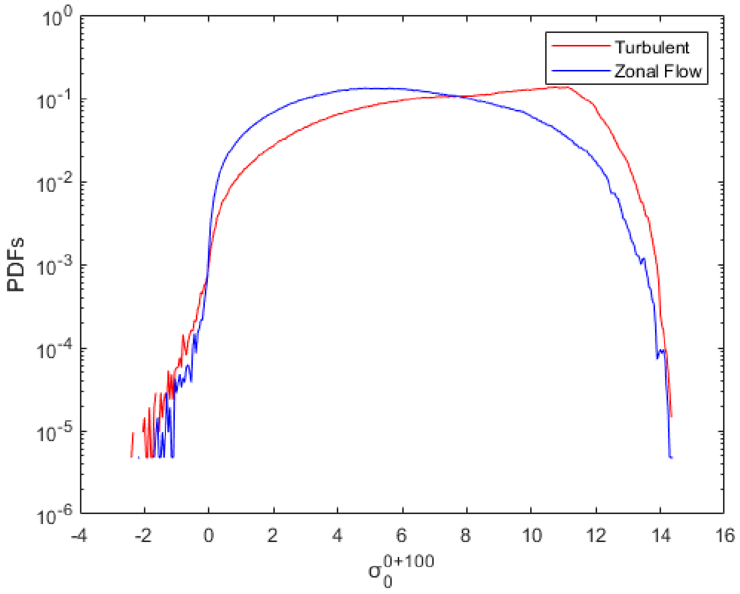

Figure 4.5. PDFs of the FTLE in the turbulent regime (red line) and the zonal flow regime (blue line) from $t = 0$ to $t = 100$ for $\tau = 100\ \Omega_{ci}^{-1}$.

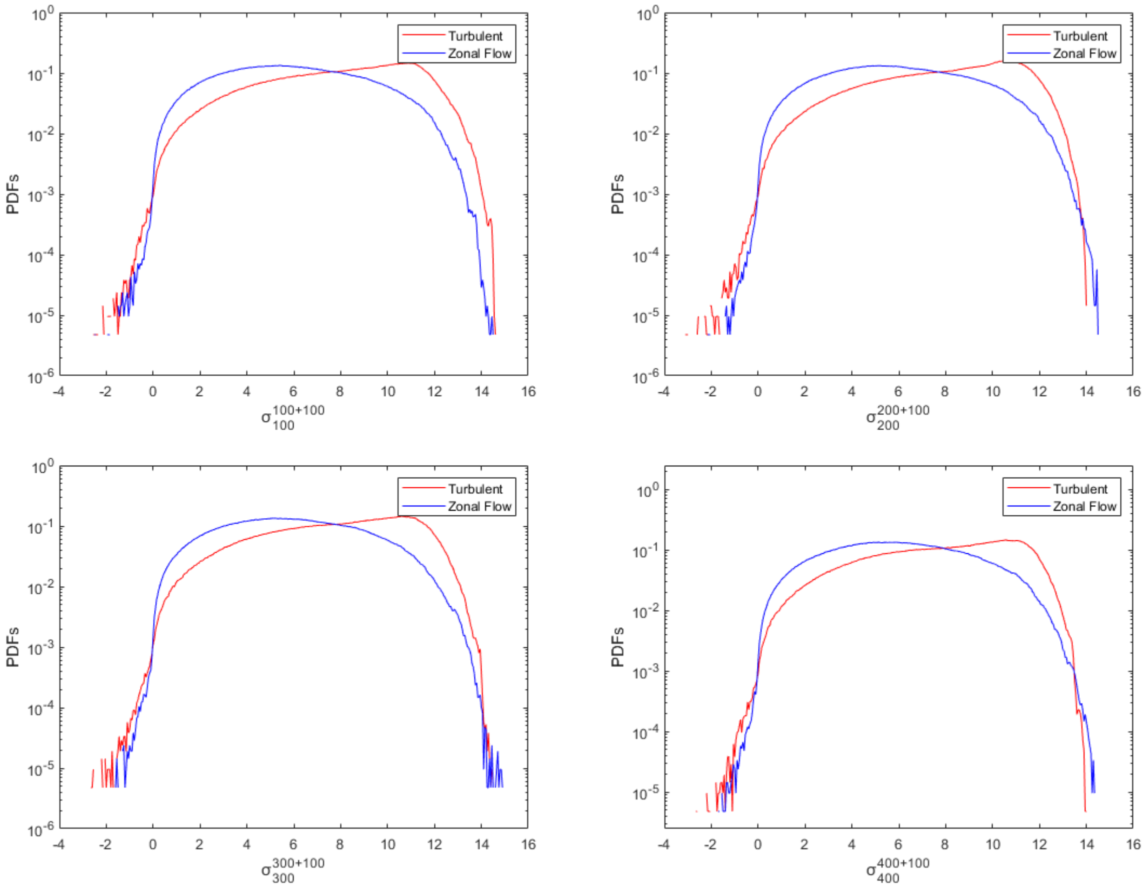

Figure 4.6. PDFs of the FTLE in the turbulent regime (red line) and the zonal flow regime (blue line) from $t = 100$ to $t = 500$.

Table 4.3. Numerical values of the variance of each PDFs for the two regimes

Time (Ω_{ci}^{-1})	Turbulent Regime	Zonal Flow
$t = 0$ to $t = 100$	8.4161	7.4551
$t = 100$ to $t = 200$	8.3485	7.4398
$t = 200$ to $t = 300$	8.0283	7.5611
$t = 300$ to $t = 400$	8.1720	7.2349
$t = 400$ to $t = 500$	8.1519	7.2515

numerical values, enhancing the interpretability of the PDFs beyond visual analysis alone, which can sometimes be more difficult to conclude. The values given for the variance further corroborate the conclusion that the zonal flow has a narrower shape than the turbulent regime. As shown in Tab. 4.3 the variances of the zonal flow are smaller than the turbulent regime. This allows us to reinforce that the zonal flow entails a less heterogeneous mixing pattern when compared to the turbulent regime, aligning with expectations stated in Beron-Vera *et al.* (2010) and Miranda *et al.* (2013).

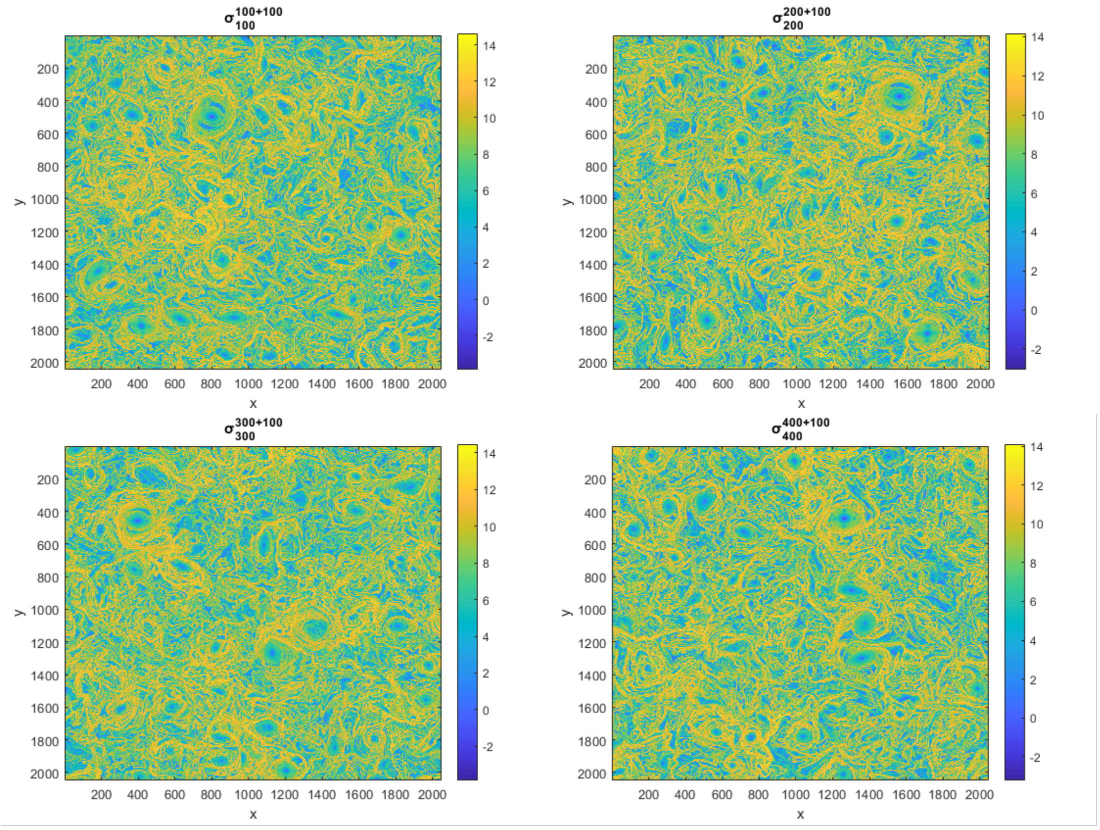

Figure 4.7. The FTLE in the turbulent regime from $t = 100$ to $t = 500$.

4.3 GEODESIC THEORY

Our analysis utilizing the Geodesic theory (Haller and Beron-Vera, 2012) is centered on identifying the closed Lagrangian shearlines referred to as elliptic barriers. The generated figures visually showcase the elliptic barriers present in both the zonal flow and turbulent regimes

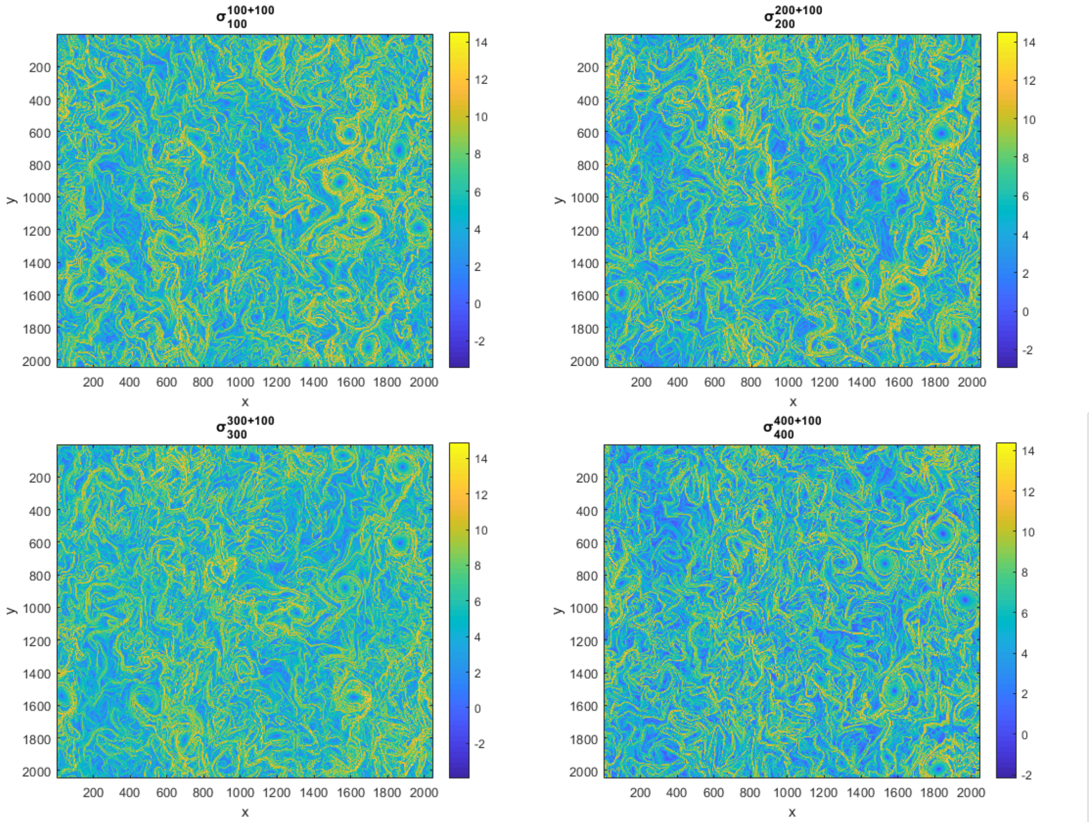

Figure 4.8. The FTLE in the zonal flow from $t = 100$ to $t = 500$.

for $t = 0$ to $t = 500$ with $\tau = 100\ \Omega_{ci}^{-1}$ (Fig.4.9, 4.12, 4.13). These elliptic barriers are considered to represent the vortices that arise due to drift wave turbulence. From these vortices, we computed their kinetic energy E_K (Eq. (3.45)) and assessed the extent to which their energy contributes to the overall kinetic energy of each domain. The results are presented in both form of figures and tables.

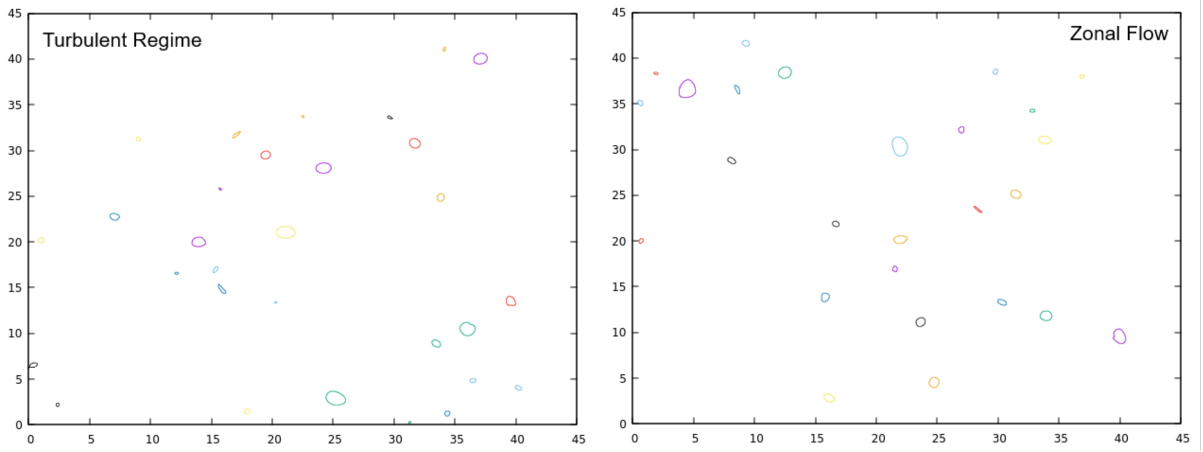

Figure 4.9. The Lagrangian shear in the turbulent regime (left panel) and zonal flow (right panel) for $t = 0$ to $t = 100$.

Figure 4.9 illustrates the presence of elliptic barriers in both the zonal flow and turbulent regimes for $t = 0$ to $t = 100$. The amount of vortices detected in each regime is 27 and 31 for

Table 4.4. Numerical values of the number of vortices present for each of the two regimes

Time (Ω_{ci}^{-1})	Turbulent Regime	Zonal Flow
$t = 0$ to $t = 100$	31	27
$t = 100$ to $t = 200$	21	22
$t = 200$ to $t = 300$	24	19
$t = 300$ to $t = 400$	27	20
$t = 400$ to $t = 500$	22	26

zonal flow and for turbulent regime, respectively (see table 4.4 for other time frames). However, the amount of vortices present is not as crucial as how much energy each vortex dissipates. For this analysis, we initially computed the kinetic energy for a single vortex (E_V) within each regime for one domain ($t = 0$ to $t = 100$). Subsequently, we determined the sum of kinetic energy released by all vortices ($E_{\sum V}$) present in each domain for each regime. These values were then compared with the total kinetic energy of the entire domain (E_{total}) for each regime and domain. The detailed values are available in Tables 4.5-4.6, and the visual representation can be found in Figures 4.10, 4.11, 4.14, 4.15.

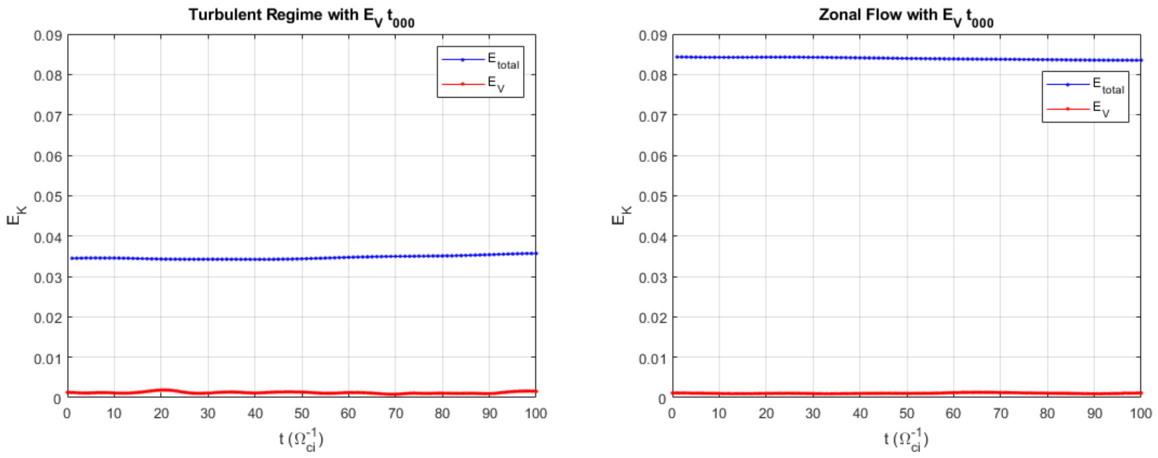

Figure 4.10. The E_{total} and E_V for the turbulent regime (left panel) and zonal flow (right panel) for $t = 0$ to $t = 100$, for one selected vortex.

Table 4.5. Numerical values of the E_{total} and E_V for the two regimes

Time (Ω_{ci}^{-1})	Turbulent Regime			Zonal Flow		
	E_{total}	E_V	$\frac{E_V}{E_{total}}$ (%)	E_{total}	E_V	$\frac{E_V}{E_{total}}$ (%)
$t = 0$ to $t = 100$	0.0347	0.0012	3.46	0.0839	0.0011	1.31

Figure 4.10 and Table 4.5 illustrate the visual and numerical values of the relationship between the total kinetic energy (E_{total}) in the domain of $t = 0$ to $t = 100$ and the kinetic energy of a single vortex (E_V) for the turbulent regime and the zonal flow. As shown in Table 4.5, a single vortex alone does not influence much of the total kinetic energy. However, when comparing both regimes, the kinetic energy present in the vortices in the turbulent regime is responsible for much more of the total kinetic energy than that of the zonal flow. This is expected, as stated in Numata *et al.* (2007), where the zonal flow absorbs the drift wave energy, so it is expected that the kinetic energy of the total domain is much higher than that of a single

vortex. This is further corroborated by the results present in figures and tables showing the relationship between $E_{\sum V}$ and E_{total}.

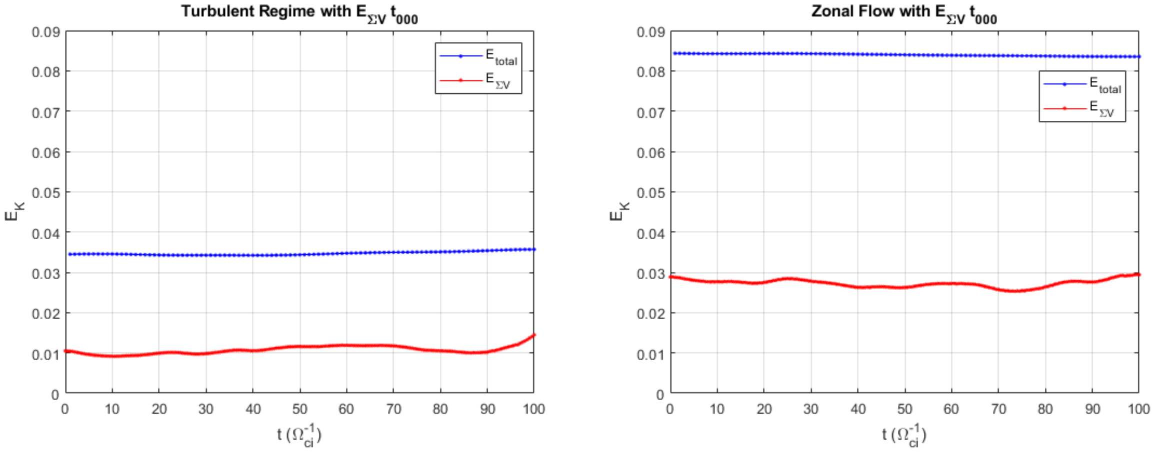

Figure 4.11. The E_{total} and $E_{\sum V}$ for the turbulent regime (left panel) and zonal flow (right panel) for $t = 0$ to $t = 100$.

Figure 4.11 presents E_{total} and $E_{\sum V}$, comparing the turbulent regime and the zonal flow side by side for the $t = 0$ to $t = 100$ domain. The corresponding results for this domain and the others are available in Table 4.6. The table illustrates that the percentage of $E_{\sum V}$ contributing to E_{total} is generally higher in the turbulent regime than in the zonal flow. This reinforces the previously mentioned from Numata *et al.* (2007) relationship between drift waves and zonal flow. The turbulent regime is dominated by drift waves, and thus, the vortices contain a substantial amount of drift wave energy. The evolution of the other domains ($t = 100$ to $t = 500$) for the turbulent regime and the zonal flow is depicted in Figures 4.14 and 4.15, respectively (note that the figures are in different scales to facilitate visualization). Similarly, the conclusions regarding the relationship between E_{total} and $E_{\sum V}$ for these domains can be drawn, that the kinetic energy contained in vortices detected represents, in general, less than half of the percentage of the total energy integrated over the whole simulation domain.

Table 4.6. Numerical values of the E_{total} and $E_{\sum V}$ for the two regimes

Time (Ω_{ci}^{-1})	Turbulent Regime			Zonal Flow		
	E_{total}	$E_{\sum V}$	$\frac{E_{\sum V}}{E_{total}}$ (%)	E_{total}	$E_{\sum V}$	$\frac{E_{\sum V}}{E_{total}}$ (%)
$t = 0$ to $t = 100$	0.0347	0.0107	30.84	0.0839	0.0273	32.54
$t = 100$ to $t = 200$	0.0361	0.0117	32.41	0.0835	0.0200	23.95
$t = 200$ to $t = 300$	0.0372	0.0191	51.34	0.0831	0.0191	22.98
$t = 300$ to $t = 400$	0.0350	0.0140	40.00	0.0828	0.0170	20.53
$t = 400$ to $t = 500$	0.0330	0.0039	11.81	0.0822	0.0264	32.12

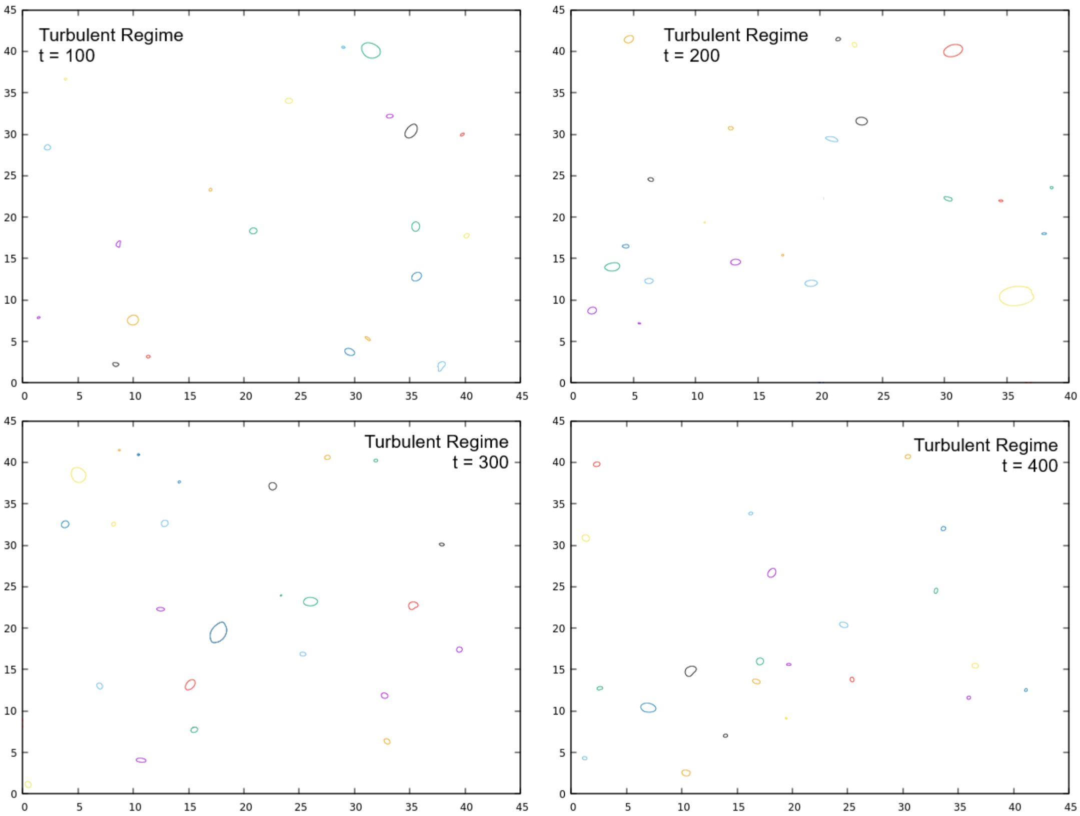

Figure 4.12. The Lagrangian shear for the turbulent regime from $t = 100$ to $t = 500$.

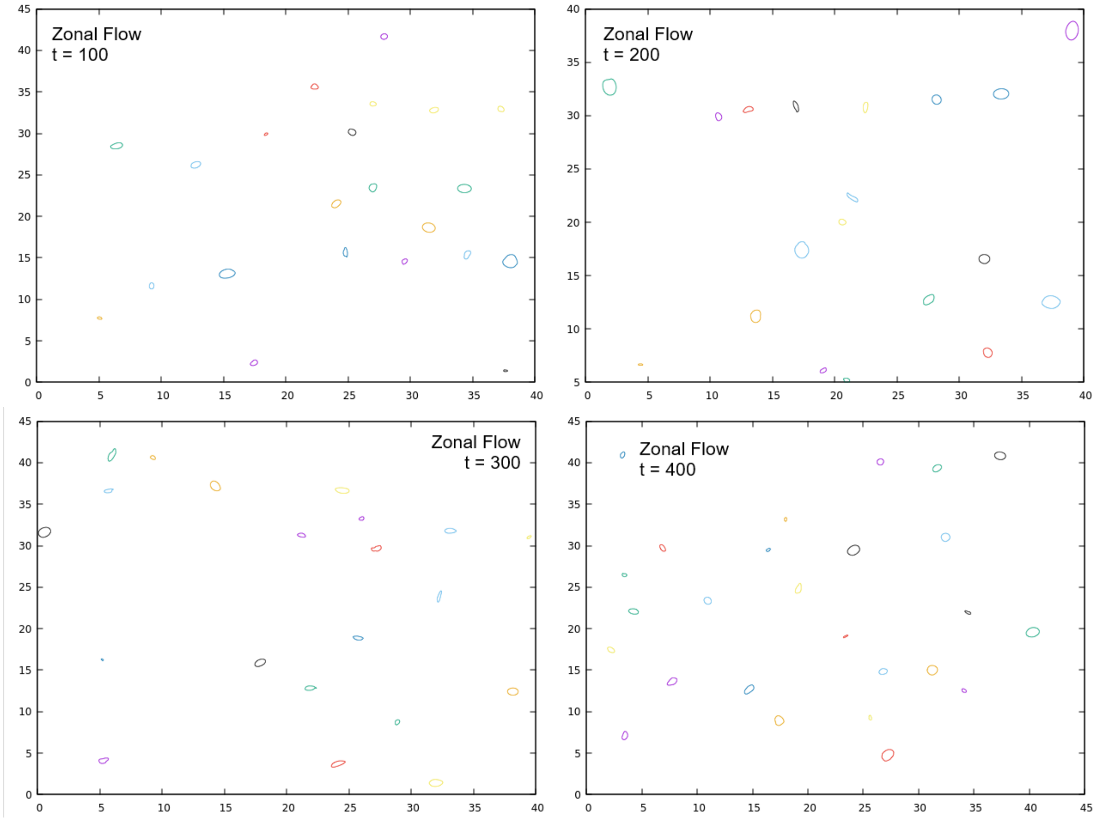

Figure 4.13. The Lagrangian shear for the zonal flow from $t = 100$ to $t = 500$.

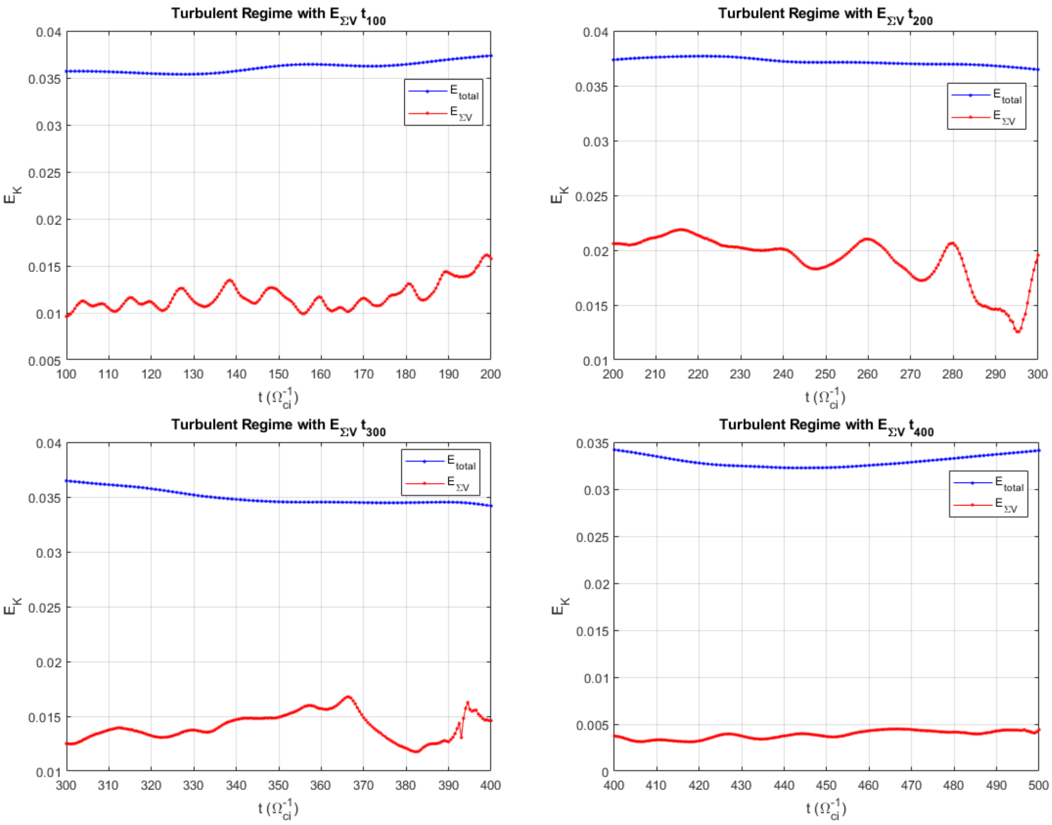

Figure 4.14. The E_{total} and $E_{\sum V}$ for the turbulent regime from $t = 100$ to $t = 500$.

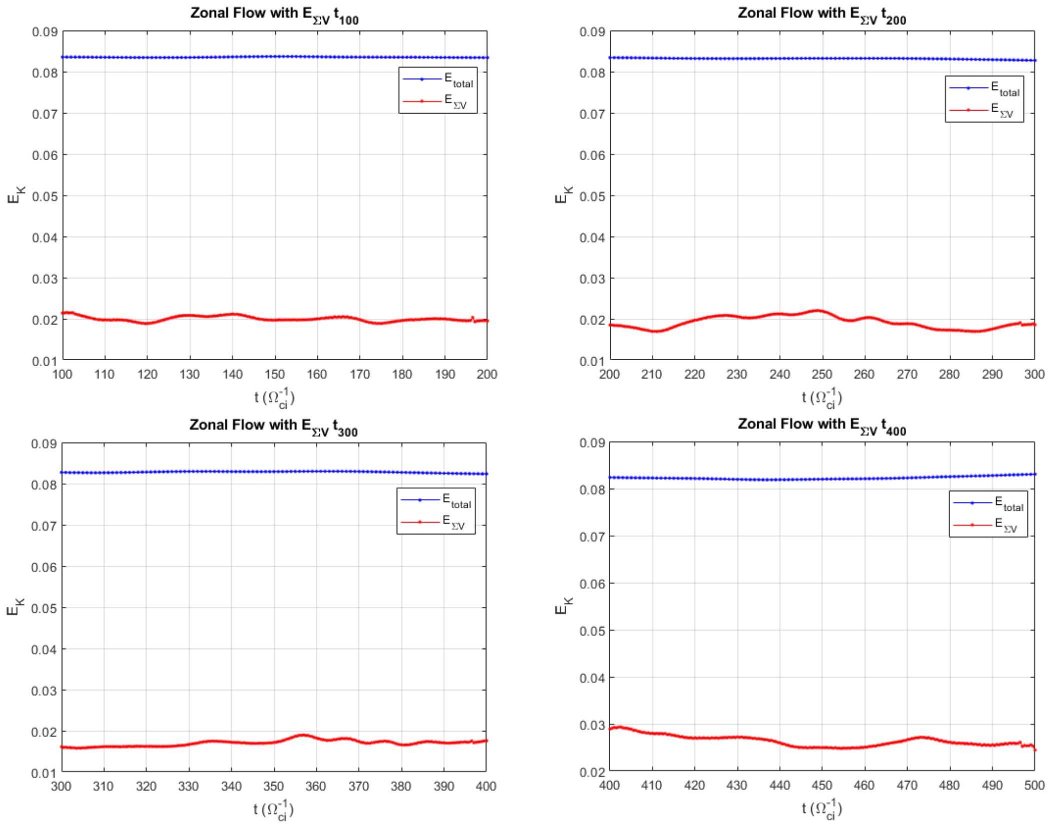

Figure 4.15. The E_{total} and $E_{\sum V}$ for the zonal flow from $t = 100$ to $t = 500$.

5 CONCLUSION

In this thesis we studied numerical simulations of the modified Hasegawa-Wakatani equations, in two different regimes, namely, a regime characterized by turbulent patterns, and a regime characterized by the presence of zonal flows. The chaotic mixing properties of the flow were elucidated by computing the finite-time Lyapunov exponents (FTLE), a commonly used tool for Lagrangian analysis of turbulent fluids. By constructing probability distribution functions of the FTLE field and comparing their shapes, we demonstrated that the turbulent regime displayed a more heterogeneous mixing behavior than the zonal flow regime. This result is consistent with the high-confinement regime associated with the zonal flow because zonal flows can suppress plasma transport in the radial direction. The radial transport is responsible for the loss of plasma particles to the walls of a tokamak (Farge *et al.*, 2006).

The computation of the FTLE represents a simple technique for the detection of Lagrangian coherent structures based on ridges of the resulting field. However, we note that ridges of the FTLE field can lead to inconsistent results (Haller, 2011). Therefore, we applied a more advanced technique, the geodesic theory (Haller and Beron-Vera, 2012). The results obtained can be summarized as follows:

- The kinetic energy contained in vortices detected by the geodesic theory represents in general less than half of the percentage of the total energy integrated over the whole simulation domain. This is in contrast with the main findings of Bos *et al.* (2008), where they find that vortices carry a large percentage of energy ($\approx$ 98%). Note, however, that they applied a technique for vortex extraction based on the wavelet transform and instantaneous snapshots of the simulation domain, i.e., an Eulerian approach, whereas the Lagrangian approach applied in this dissertation guarantees that vortices remain coherent over a finite-time period.
- The percentage of kinetic energy contained in vortices is, in general, higher in the turbulent regime compared to the zonal-flow regime. The results are in agreement with the general characteristics of a fusion plasma during a low-to-high transition. In the low containment regime, turbulence can carry particles and energy radially toward the walls, whereas the high containment regime is characterized by a decrease in the radial flux of particle and energy in the direction of the reactor's wall.

The methodologies and understandings derived from our study may aid in the comprehension of drift-wave-induced turbulence in tokamak plasmas. Future work could incorporate integrating the enstrophy within vortices, and the flux of mass as defined by Bos *et al.* (2008). The techniques applied in this thesis are transferable to turbulent flows prevalent in fluid mechanics, such as pipe flows, airfoils, and aerodynamics. Consequently, the application of Lagrangian techniques has the capacity to advance our comprehension of turbulent flows in engineering contexts.

REFERENCE LIST

Anderson, J. and Hnat, B. (2017). Statistical analysis of hasegawa-wakatani turbulence. *Physics of Plasmas*, 24.

Beron-Vera, F. J., Olascoaga, M. J., and Goni, G. J. (2010). Surface ocean mixing inferred from different multisatellite altimetry measurements. *Journal of Physical Oceanography*, 40:2466–2480.

Bishop, C. (1986). Stability of localized mhd modes in divertor tokamaks – a picture of the h-mode. *Nuclear Fusion*, 26(8):1063.

Bittencourt, J. (2004). *Fundamentals of Plasma Physics*. Springer New York.

Bos, W. J., Futatani, S., Benkadda, S., Farge, M., and Schneider, K. (2008). The role of coherent vorticity in turbulent transport in resistive drift-wave turbulence. *Physics of Plasmas*, 15.

Burden, R. L. and Faires, J. D. (2011). *Numerical analysis*. Brooks/Cole Cengage Learning.

Burrell, K. H. (1997). Effects of E×B velocity shear and magnetic shear on turbulence and transport in magnetic confinement devices. *Physics of Plasmas*, 4(5):1499–1518.

Chen, F. F. (2016). *Introduction to Plasma Physics and Controlled Fusion*. Springer International Publishing Switzerland, Los Angeles, CA, U.S.A.

Connor, J. W. and Wilson, H. R. (2000). A review of theories of the l-h transition. *Plasma Physics and Controlled Fusion*, 42(1):R1.

Crepaldi, C. (2021). Busca por evidências de dinâmica caótica nas flutuações turbulentas de densidade em plasmas.

D'Angelo, N. (1961). Low-frequency oscillations in cesium thermionic converters. *Physics of Fluids (U.S.)*, 4(8).

Davidson, P. A. (2015). *Turbulence: an introduction for scientists and engineers*. Oxford university press.

Dendy, R. (1990). *Plasma Dynamics*. Oxford science publications. Clarendon Press.

Dewhurst, J. M. (2010). *Statistical Description and Modelling of Fusion Plasma Edge Turbulence*. PhD thesis, University of Warwick, England.

Diamond, P. H., Itoh, S.-I., Itoh, K., and Hahm, T. S. (2005). Zonal flows in plasma—a review. *Plasma Physics and Controlled Fusion*, 47(5):R35.

Diamond, P. H., Liang, Y.-M., Carreras, B. A., and Terry, P. W. (1994). Self-regulating shear flow turbulence: A paradigm for the l to h transition. *Phys. Rev. Lett.*, 72:2565–2568.

Farazmand, M. and Haller, G. (2012). Computing Lagrangian coherent structures from their variational theory. *Chaos: An Interdisciplinary Journal of Nonlinear Science*, 22(1):013128.

Farge, M., Schneider, K., and Devynck, P. (2006). Extraction of coherent bursts from turbulent edge plasma in magnetic fusion devices using orthogonal wavelets. *Physics of Plasmas*, 13.

Furth, H. P. (1975). Tokamak research. *Nuclear Fusion*, 15(3):487.

Gallagher, S. J. (2013). *Zonal flow generation through four wave interaction in reduced models of fusion plasma turbulence*. PhD thesis, University of Warwick.

Gilat, A. and Subramaniam, V. (2013). *Numerical Methods for Engineers and Scientists: An Introduction with Applications Using MATLAB*. Wiley, Massachusetts, USA, 3rd edição.

Haller, G. (2001). Distinguished material surfaces and coherent structures in three-dimensional fluid flows. *Physica D: Nonlinear Phenomena*, 149(4):248–277.

Haller, G. (2011). A variational theory of hyperbolic lagrangian coherent structures. *Physica D: Nonlinear Phenomena*, 240:574–598.

Haller, G. and Beron-Vera, F. J. (2012). Geodesic theory of transport barriers in two-dimensional flows. *Physica D: Nonlinear Phenomena*, 241:1680–1702.

Haller, G. and Yuan, G. (2000). Lagrangian coherent structures and mixing in two-dimensional turbulence. *Physica D: Nonlinear Phenomena*, 147(3):352–370.

Hasegawa, A. and Mima, K. (1978). Pseudo-three-dimensional turbulence in magnetized nonuniform plasma. *The Physics of Fluids*, 21(1):87–92.

Hasegawa, A. and Wakatani, M. (1983). Plasma edge turbulence. *Phys. Rev. Lett.*, 50:682–686.

Hasegawa, A. and Wakatani, M. (1987). Self-organization of electrostatic turbulence in a cylindrical plasma. *Phys. Rev. Lett.*, 59:1581–1584.

Hazeltine, R. and Meiss, J. (2003). *Plasma Confinement*. Dover books on physics. Dover Publications.

Hinton, F. L. and Hazeltine, R. D. (1976). Theory of plasma transport in toroidal confinement systems. *Rev. Mod. Phys.*, 48:239–308.

Horton, W. (1990). Nonlinear drift waves and transport in magnetized plasma. *Physics Reports*, 192(1):1–177.

Jenko, F., Dorland, W., Kotschenreuther, M., and Rogers, B. N. (2000). Electron temperature gradient driven turbulence. *Physics of Plasmas*, 7(5):1904–1910.

Kadomtsev, B. B. (1988). Evolution of the tokamak. *Plasma Physics and Controlled Fusion*, 30(14):2031.

Kikuchi, M., Lackner, K., Tran, M. Q., and Agency., I. A. E. (2012). *Fusion physics*. International Atomic Energy Agency.

Kim, E.-j. and Diamond, P. H. (2003). Zonal flows and transient dynamics of the $l-h$ transition. *Phys. Rev. Lett.*, 90:185006.

Kubic, M. (2012). Experimental study of the edge plasma of the tore supra tokamak.

Lashinsky, H. (1964). Universal instability in a fully ionized inhomogeneous plasma. *Phys. Rev. Lett.*, 12:121–123.

Lawson, J. D. (1957). Some criteria for a power producing thermonuclear reactor. *Proc. Phys. Soc. (London)*, 70(1):6.

Lekien, F., Shadden, S. C., and Marsden, J. E. (2007). Lagrangian coherent structures in n-dimensional systems. *Journal of Mathematical Physics*, 48(6):065404.

LeVeque, R. J. (2005). *Finite Difference Methods for Differential Equations*. Amath 585–6 notes, University of Washington.

Mazzucato, E. (1976). Small-scale density fluctuations in the adiabatic toroidal compressor. *Phys. Rev. Lett.*, 36:792–794.

Mima, K. and Hasegawa, A. (1977). Stationary spectrum of strong turbulence in magnetized nonuniform plasma. *Phys. Rev. Lett.*, 39:205–208.

Miranda, R. A., Rempel, E. L., Chian, A. C.-L., Seehafer, N., Toledo, B. A., and Munoz, P. R. (2013). Lagrangian coherent structures at the onset of hyperchaos in the two-dimensional navier-stokes equations. *Chaos: An Interdisciplinary Journal of Nonlinear Science*, 23(3).

Moyer, R. A., Burrell, K. H., Carlstrom, T. N., Coda, S., Conn, R. W., Doyle, E. J., Gohil, P., Groebner, R. J., Kim, J., Lehmer, R., Peebles, W. A., Porkolab, M., Rettig, C. L., Rhodes, T. L., Seraydarian, R. P., Stockdale, R., Thomas, D. M., Tynan, G. R., and Watkins, J. G. (1995). Beyond paradigm: Turbulence, transport, and the origin of the radial electric field in low to high confinement mode transitions in the DIII-D tokamak. *Physics of Plasmas*, 2(6):2397–2407.

Numata, R., Ball, R., and Dewar, R. L. (2007). Bifurcation in electrostatic resistive drift wave turbulence. *Physics of Plasmas*, 14.

Ottino, J. M. (1989). *The kinematics of mixing: stretching, chaos, and transport*, volume 3. Cambridge University Press, Cambridge.

Padberg, K., Hauff, T., Jenko, F., and Junge, O. (2007). Lagrangian structures and transport in turbulent magnetized plasmas. *New Journal of Physics*, 9(11):400.

Peacock, T. and Haller, G. (2013). Lagrangian coherent structures: The hidden skeleton of fluid flows. *Physics Today*, 66:41–47.

Pierrehumbert, R. T. and Yang, H. (1993). Global chaotic mixing on isentropic surfaces. *Journal of the atmospheric sciences*, 50(15):2462–2480.

Pushkarev, A. (2013). *Self-organization of isotopic and drift-ware turbulence*. PhD thesis, Ecully, Ecole centrale de Lyon.

Rogers, B. N., Dorland, W., and Kotschenreuther, M. (2000). Generation and stability of zonal flows in ion-temperature-gradient mode turbulence. *Phys. Rev. Lett.*, 85:5336–5339.

Rogers, B. N., Drake, J. F., and Zeiler, A. (1998). Phase space of tokamak edge turbulence, the $L-H$ transition, and the formation of the edge pedestal. *Phys. Rev. Lett.*, 81:4396–4399.

Schaub, H., Parker, G., and King, L. (2006). Coulomb thrusting application study. página 120.

Shadden, S. C., Lekien, F., and Marsden, J. E. (2005). Definition and properties of lagrangian coherent structures from finite-time lyapunov exponents in two-dimensional aperiodic flows. *Physica D: Nonlinear Phenomena*, 212:271–304.

Smith, C. L. and Cowley, S. (2010). The path to fusion power¡sup¿†¡/sup¿. *Philosophical Transactions of the Royal Society A: Mathematical, Physical and Engineering Sciences*, 368(1914):1091–1108.

Souza, J. H. C. d. (2012). *Estudos de esterilização por plasma a pressão atmosférica*. PhD thesis, University of Brasília.

Stangeby, P. C. *et al.* (2000). *The plasma boundary of magnetic fusion devices*, volume 224. Institute of Physics Pub. Philadelphia, Pennsylvania.

Truesdell, C., Noll, W., Truesdell, C., and Noll, W. (2004). *The non-linear field theories of mechanics*. Springer, New York, USA.

Wagner, F., Becker, G., Behringer, K., Campbell, D., Eberhagen, A., Engelhardt, W., Fussmann, G., Gehre, O., Gernhardt, J., Gierke, G. v., Haas, G., Huang, M., Karger, F., Keilhacker, M., Klüber, O., Kornherr, M., Lackner, K., Lisitano, G., Lister, G. G., Mayer, H. M., Meisel, D., Müller, E. R., Murmann, H., Niedermeyer, H., Poschenrieder, W., Rapp, H., Röhr, H., Schneider, F., Siller, G., Speth, E., Stäbler, A., Steuer, K. H., Venus, G., Vollmer, O., and Yü, Z. (1982). Regime of improved confinement and high beta in neutral-beam-heated divertor discharges of the asdex tokamak. *Phys. Rev. Lett.*, 49:1408–1412.

Wakatani, M. and Hasegawa, A. (1984). A collisional drift wave description of plasma edge turbulence. *Physics of Fluids*, 27:611–618.

Weiland, J. (2000). Collective modes in inhomogeneous plasma: Kinetic and advanced fluid theory iop. *Bristol, Philadelphia*.

Wesson, J. and Campbell, D. (2004). *Tokamaks*. International series of monographs on physics. Clarendon Press.

XU, G. and WU, X. (2017). Understanding l–h transition in tokamak fusion plasmas*. *Plasma Science and Technology*, 19(3):033001.

Young, H., Freedman, R., and Ford, A. (2012). *Sears and Zemansky's University Physics: With Modern Physics*. Addison-Wesley.

Zohm, H. (2014). *Magnetohydrodynamic Stability of Tokamaks*. Wiley.